Satellite spectra for heliumlike titanium. II

M. Bitter, K. W. Hill, M. Zarnstorff, S. von Goeler, R. Hulse, L. C. Johnson, N. R. Sauthoff,
S. Sesnic, and K. M. Young

Plasma Physics Laboratory, Princeton University, Princeton, New Jersey 08544

M. Tavernier

Institut Curie, Université Pierre et Marie Curie, 75231 Paris, France

F. Bely-Dubau and P. Faucher

Observatoire de Nice, Boîte Postale No. 139, 06003 Nice Cédex, France

M. Cornille and J. Dubau

Observatoire de Paris, 92195 Meudon, France

(Received 8 July 1985)

$K\alpha$ x-ray spectra of heliumlike titanium, Ti XXI, from Tokamak Fusion Test Reactor (TFTR) plasmas have been observed with a high-resolution crystal spectrometer and have been used as a diagnostic of central plasma parameters. The data allow detailed comparison with recent theoretical predictions for the Ti XXI heliumlike lines and the associated satellite spectrum in the wavelength range from 2.6000 to 2.6400 Å. Improved values for the excitation rate coefficients of the Ti XXI resonance line, the intercombination lines, and the forbidden line, and new theoretical results on the wavelengths and transition probabilities for berylliumlike satellites due to transitions of the type $1s^2 2lnl'$-$1s 2p 2l''nl'''$ with $n = 2$–4 have been calculated. These data complement the theory given in an earlier paper [F. Bely-Dubau *et al.*, Phys. Rev. A **26**, 3459 (1982)]. The experimental data are in excellent agreement with the theoretical predictions for the entire satellite spectrum. For plasmas with electron temperatures, T_e, in the range from 1.2 to 1.8 keV, there is also good general agreement between theory and experiment for the heliumlike lines of Ti XXI. The observed intensity ratios of the intercombination and forbidden lines to the resonance line are, however, larger than the predicted values by as much as an order of magnitude for electron temperatures $T_e < 1.2$ keV. The enhancement of these lines is correlated with the abundance of lithiumlike titanium. The experimental data indicate that still other atomic processes, in addition to those considered by the theory, are important for the excitation of these lines. The experimental results are documented to stimulate further analysis. The observed wavelengths agree to within an uncertainty of 0.5 mÅ with predictions from calculations which include relativistic and radiative corrections up to the third order in α. The central ion temperature and the central toroidal rotation velocity of TFTR plasmas with ohmic and neutral beam heating were obtained from Doppler measurements of the Ti XXI resonance line. Wavelength shifts of the apparent resonance line profile due to unresolved dielectronic satellites, which can be important corrections to Doppler-shift measurements of plasma rotation velocities, have been determined as a function of the ion and electron temperatures and the fitting limits. Results on the electron temperature and the relative charge-state density of lithiumlike and heliumlike titanium were derived from the satellite spectrum and have been interpreted with plasma modeling. These results are of interest for the determination of the ionization equilibrium and the impurity transport.

I. INTRODUCTION

In a previous paper[1] we presented x-ray spectra of heliumlike titanium, Ti XXI, from tokamak plasmas produced in the Poloidal Divertor Experiment (PDX) and gave a detailed comparison between experiment and theory for the spectral range from 2.6075 to 2.6165 Å, which includes the Ti XXI $1s^2 {}^1S_0$-$1s 2p {}^1P_1$ resonance line and the dielectronic satellites in the immediate neighborhood of the resonance line due to transitions of the type $1s^2 nl$-$1s 2pnl$ with $n \geq 3$. The theoretical predictions were in excellent agreement with the experimental data, indicating that the two considered processes of line excitation, i.e.,

dielectronic recombination (for the $n \geq 3$ satellites) and direct electron impact excitation (for the $1s^2 {}^1S_0$-$1s 2p {}^1P_1$ resonance line), adequately describe the observations. The satellite spectra of hydrogenlike titanium, Ti XXII, also were shown previously to be fully determined by these two processes.[2]

In this paper we present new data on the satellite spectra of Ti XXI which have been observed from Tokamak Fusion Test Reactor (TFTR) plasmas with a high-resolution Bragg crystal spectrometer. These data allow us to extend the comparison between theory and experiment to the wavelength range from 2.6165 to 2.6400 Å, which includes the intercombination and forbidden heli-

umlike lines, $1s^2\,{}^1S_0-1s\,2p\,{}^3P_{1,2}$ and $1s^2\,{}^1S_0-1s\,2s\,{}^3S_1$, and the lithiumlike satellites, $1s^2nl$-$1s\,2pnl$ with $n=2$, as well as berylliumlike satellites due to transitions of the type $1s^2 2lnl'$-$1s\,2p\,2l''nl'''$ with $n\geq 2$. The theory of these spectral lines is more complex since additional processes of line excitation have to be considered. In addition to electron impact excitation, the upper levels, $1s\,2p\,{}^1P_1,{}^3P_{1,2}$ and $1s\,2s\,{}^3S_1$, of the heliumlike lines can be populated by recombination of hydrogenlike titanium, Ti XXII, and inner-shell ionization of lithiumlike titanium, Ti XX. These processes are especially important for the population of the ${}^3P_{1,2}$ and ${}^3S_1$ levels and have been invoked to explain recent data from solar observations[3,4] and Alcator-*C* tokamak plasmas.[5,6] Furthermore, collisional inner-shell excitation of lithiumlike titanium, in addition to dielectronic recombination of Ti XXI, is an important mechanism of excitation for satellite transitions of the type $1s^2 2s$-$1s\,2s\,2p$. The contributions from these two processes to the satellite spectrum have been described in detail in our previous publication.[1] Here we present improved values for the excitation rate coefficients of the heliumlike lines of Ti XXI which include the contributions from radiative cascade transitions, collisional resonances, recombination of hydrogenlike titanium, and inner-shell ionization of lithiumlike titanium. We also report new theoretical results on the wavelengths and transition probabilities for the berylliumlike satellites: $1s^2 2lnl'$-$1s\,2p\,2l''nl'''$ with $n=2-4$. These new theoretical results and the atomic data in Refs. 1 and 7 are used for a detailed comparison with the experimental observations. We find that the theoretical predictions for the Ti XXI resonance line and the entire satellite spectrum are in very good agreement with the experimental data. This indicates that the satellite features are well described by the two processes of dielectronic recombination and inner-shell excitation. On the other hand, we find that the theory does not fully describe the observed intensities of the intercombination and forbidden lines of Ti XXI. Partial agreement between predicted and observed intensities is obtained for electron temperatures T_e above 1.2 keV. However, the observed intensities are larger than the predicted values by as much as 1 order of magnitude for $T_e < 1.2$ keV. The experimental data show a strong correlation between the intensities of the intercombination and forbidden lines and the abundance of lithiumlike titanium. The theoretically predicted contribution from inner-shell ionization of Ti XX to the intensity of the forbidden line is too small to account for the observed intensities. Although we examined several atomic processes, we have not yet resolved these discrepancies.

The spectra of high-Z heliumlike and hydrogenlike ions have important applications in the diagnosis of hot plasmas. In particular, they have been used for the diagnosis of solar events[3,4,8-12] and tokamak plasmas.[13-20] The applications include measurement of the central ion temperature[15,16] and toroidal plasma rotation velocity[19] from the observed Doppler broadening and Doppler shift of the resonance line, measurement of the central electron temperature from the intensity of the dielectronic satellites,[3,4,8-12,15-17] and determination of the ionization equilibrium and ion transport from the intensity of the

collisionally excited satellites.[14,20] The intensity ratios of the heliumlike lines, i.e., the resonance, intercombination, and forbidden lines, are used for measurement of the electron density in solar flares.[21,22]

A detailed comparison between theory and experiment is of great interest in view of these diagnostic applications. We document our experimental results carefully in order to stimulate new theoretical analyses of the still existing discrepancies between the predicted and observed intensities of the intercombination and forbidden lines of Ti XXI.

The paper is organized as follows. The plasma parameters and the experimental apparatus are described in Sec. II. A detailed comparison of the observed satellite spectra of Ti XXI with the theoretical predictions is given in Sec. III. Experimental and theoretical wavelengths are compared in Sec. IV. The remaining discrepancies between observed and predicted intensities of the heliumlike lines are discussed in Sec. V. Rate coefficients for excitation of the heliumlike lines of Ti XXI, and theoretical results on wavelengths, line factors, and transition probabilities for the berylliumlike satellites are presented in Secs. VI and VII. In Sec. VIII we describe diagnostic applications and present experimental results from the TFTR tokamak plasmas. A summary of the results and conclusions are presented in Sec. IX.

II. EXPERIMENTAL CONDITIONS AND EQUIPMENT

The experiments have been performed on the TFTR, which was designed to study a hydrogenic plasma at fusion breakeven parameters. Toroidal plasmas with major radius R of 2.00–3.00 m, minor radius a of 0.40–0.83 m, and central electron densities $n_e(0)$ of $(0.1-1)\times 10^{20}$ m^{-3} are produced in a TFTR discharge by a toroidal current I_p in the range from 0.25 to 2.5 MA. The plasma current raises the central ion and electron temperatures, $T_i(0)$ and $T_e(0)$, to 1–4 keV by Ohmic heating. Auxiliary heating by injection of intense neutral hydrogenic beams, at power levels up to 27 MW, and adiabatic compression will be available also to further heat the plasma to reactor relevant temperatures near 10 keV. The plasma is contained in a toroidal magnetic field having a maximum strength of 5.2 T. The major and minor plasma radii are adjusted by the equilibrium magnetic field and by means of movable carbon limiters.

The experimental data have been obtained mainly from Ohmic discharges which were extensively studied in confinement scaling experiments during the first two phases of machine operation. These discharges had $R=2.55$ or 2.64 m and $a=0.42$, 0.55, 0.83 m, I_p ranging from 0.8 to 1.4 MA, central electron densities of $(1-6)\times 10^{19}$ m^{-3}, and $T_i(0)$ and $T_e(0)$ in the range from 0.5 to 2 keV. The plasmas were in quasi-steady-state conditions for periods of 2–3 sec. The characteristic energy confinement time was typically 0.1 to 0.3 sec. Some experimental results from the first TFTR experiments with neutral beam injection were also obtained.

TFTR plasmas are intense sources of soft-x-ray radiation. A typical soft-x-ray spectrum is shown in Fig. 1(a). The data were recorded by the x-ray pulse-height analysis
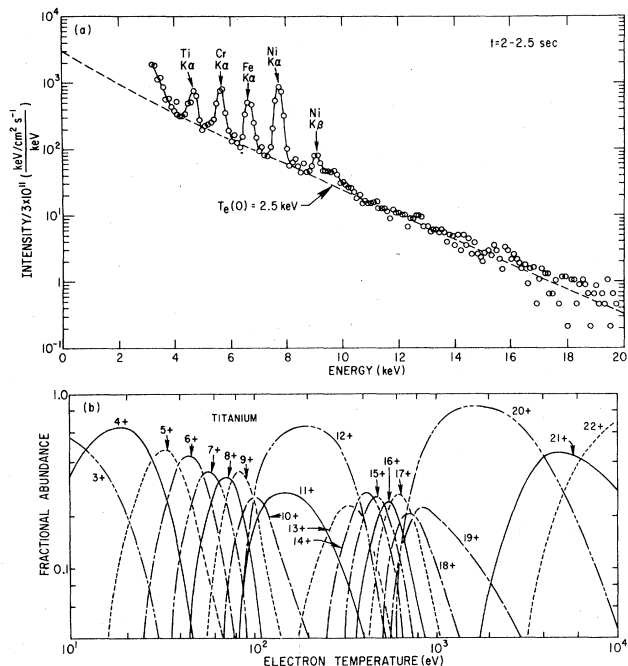
FIG. 1. (a) Soft-x-ray spectrum emitted from an Ohmically heated hydrogen plasma of a TFTR discharge. Spectrum shows a bremsstrahlung and recombination continuum and the characteristic $K\alpha$ line radiation from metal impurity ions of Ti, Cr, Fe, and Ni, the constituents of the plasma limiter and the vacuum vessel. Data have been recorded by the pulse-height analysis system, which has an energy resolution of 220 eV at 6 keV. (b) Fractional abundances of the ion charge states of titanium for coronal equilibrium as calculated by Breton et al. (Ref. 25).

(PHA) system[23] from a discharge with $I_p = 1$ MA. The spectrum consists of a bremsstrahlung and recombination continuum and $K\alpha$ line radiation from metal impurity ions of titanium, chromium, iron, and nickel, which are the constituents of the vacuum vessel and plasma limiter. Traces of these metals are present in TFTR plasmas. Their concentration is determined by the processes of plasma-wall interaction and transport processes which determine the impurity confinement in the plasma. The impurity concentration is thus dependent on the experimental parameters, such as plasma current, electron density, and electron temperature.[24] The electron temperature is inferred from the slope of the soft-x-ray continuum, and the concentration of metal impurities is determined from the observed intensity of the $K\alpha$ radiation.

The energy resolution of the PHA system is not sufficient to resolve the spectral components emitted from the different ion species or charge states of an element. Interpretation of the measurements shown in Fig. 1(a) is thus usually based on certain assumptions about the state of ionization of the metal impurities and the spatial distribution of the ion charge states which, together with the electron density and electron temperature profiles, determine the intensity of the ion line spectra. In general, one may assume that the metal impurity ions reach an ionization equilibrium since the ionization and recombination times of typically 10—30 ms are short compared with the period of steady-state conditions in large tokamak plasmas. This

equilibrium distribution differs from that expected in coronal ionization equilibrium, however, as a result of radial ion transport and charge-exchange recombination with neutral hydrogen. Nevertheless, the coronal equilibrium can be used for an approximate description of the ion distribution in tokamak plasmas. Figure 1(b) shows the fractional abundances of titanium charge states for coronal equilibrium as calculated by Breton et al.[25] According to these calculations, heliumlike titanium, Ti XXI, is the dominant state of ionization for the wide range of electron temperature from 0.8 to 4 keV. This can be explained by the large difference of the ionization potentials for lithiumlike and heliumlike titanium ions. Expected deviations from coronal equilibrium will be discussed further in Sec. VIII.

Recent experimental investigations of the titanium charge-state distribution in tokamak plasmas produced by the Princeton Large Torus (PLT) have been consistent, in general, with theoretically predicted ionization equilibria. The measurements were performed with a Johann-type curved-crystal spectrometer.[26] The instrument had a spectral resolution of $\lambda/\Delta\lambda = 5000$ at $\lambda = 2.6$ Å and permitted simultaneous observation of the characteristic $K\alpha$ line radiation from all the titanium charge states. Figure 2 shows a time sequence of 14 titanium spectra which were recorded with a time resolution of 60 ms from PLT discharges with auxiliary ion cyclotron heating. A maximum central electron temperature of 2 keV was obtained during the rf heating pulse from 400 to 550 msec. We infer from Fig. 2 that titanium is very rapidly ionized to the heliumlike charge state in these tokamak plasmas. The radiation from lithiumlike titanium, Ti XX, and lower charge states is appreciable during short time intervals of ~120 msec at the beginning and the end of a discharge. Radiation from hydrogenlike titanium, Ti XXII, is observed when the electron temperature rises to 2 keV. However, the intensity of this radiation is very weak and
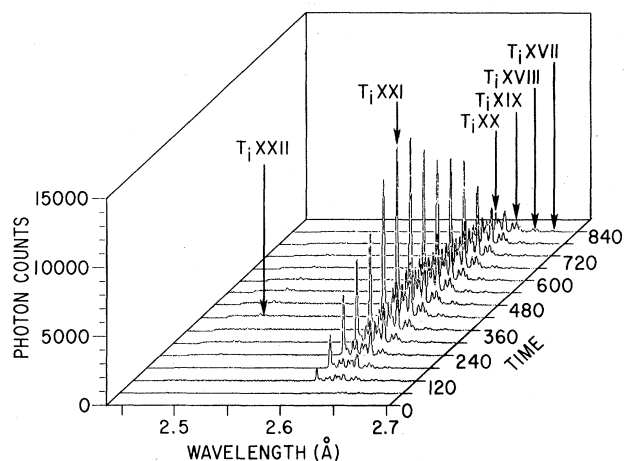

FIG. 2. $K\alpha$ line spectrum of titanium ions Ti XVII—Ti XXII as observed by means of a curved-crystal spectrometer from Princeton Large Torus discharges with auxiliary ion cyclotron heating. Spectra have been recorded during consecutive time intervals of 60 ms. A maximum central electron temperature of 2 keV was obtained during the rf heating pulse from 400 to 600 ms.

barely resolved from the bremsstrahlung and recombination continuum. The spectra shown in Fig. 2 thus confirm the assumptions made in the discussion of the previously obtained high-resolution spectra of Ti XXII.[2] Since both the theoretical and experimental observations indicate that heliumlike titanium is the dominant state of ionization for a wide range of central electron temperatures, we have chosen to use the Ti XXI $K\alpha$ radiation as a diagnostic for central TFTR plasma parameters.

The x-ray spectrometer used on TFTR has been described earlier.[27] It is similar to the instruments installed on the PLT and the PDX. The spectrometer consists of a quartz $(20\overline{2}3)$ crystal of dimensions 1.5 in. $\times 6$ in., which is bent to a radius of curvature of 373 cm, and a position-sensitive detector in the Johann configuration. The crystal views horizontally across the central midplane of the TFTR through a 0.005-in.-thick beryllium window. X rays transmitted through helium at 1 atmosphere are diffracted onto a 10 cm $\times$ 18 cm position-sensitive multiwire proportional counter. The detector counts the x-ray photons and encodes their position along the 18-cm di-

mension to an accuracy of 0.25 mm full width at half maximum (FWHM). This position information translates to Bragg diffraction angle and, hence, to x-ray wavelength. The Bragg angle, crystal diffraction properties, distance from crystal to detector, and detector position resolution are chosen to yield a spectral resolving power $\lambda/\Delta\lambda$ of 25 000. Up to 128 spectra can be recorded during a discharge with integration time selectable from 1 to 1000 ms. The line of sight from the crystal into the plasma makes an angle of 22° with respect to the radial direction at the magnetic axis (the center of the TFTR vacuum vessel) so that 37% of the toroidal plasma rotation velocity can be measured from the observed Doppler shift of the spectral lines.

III. COMPOSITION OF THE TITANIUM LINE SPECTRA

In this section we discuss the contributions from various excitation processes and compare the experimental data with theoretical predictions. Details of this compar-
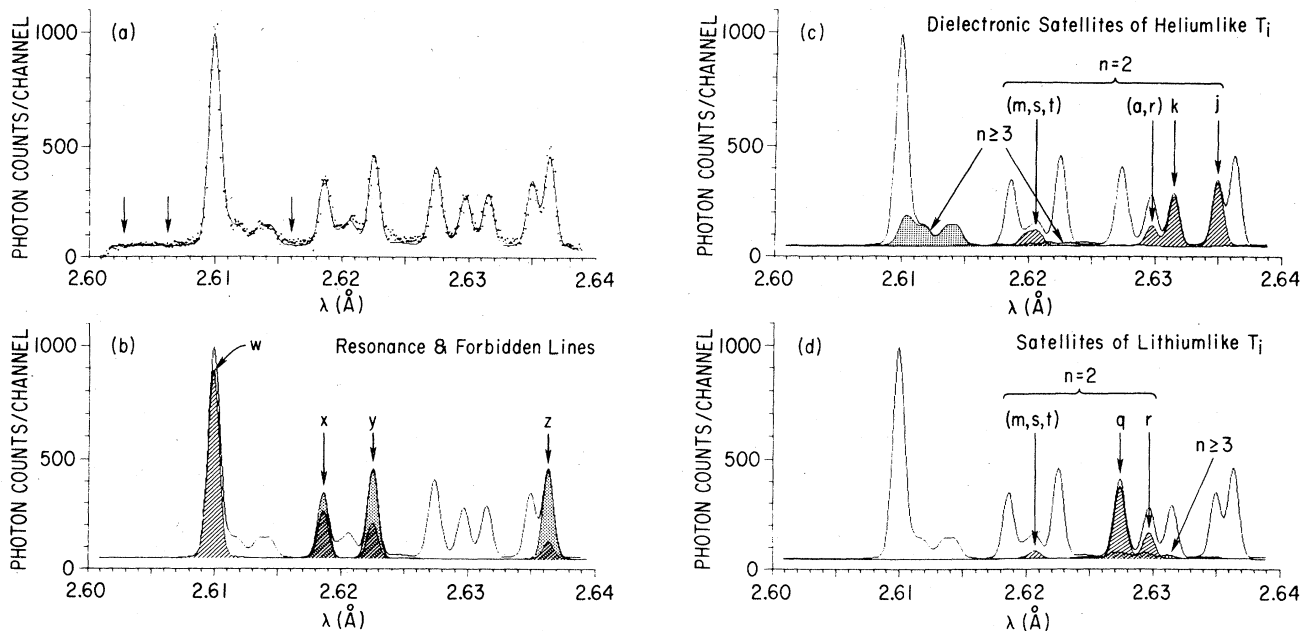

FIG. 3. (a) Satellite spectra of Ti XXI, Ti XX, and Ti XIX. Experimental data which are represented by the dotted curve have been recorded from Ohmically heated plasmas of TFTR discharges with a Bragg crystal spectrometer of high resolution ($\lambda/\Delta\lambda = 25\,000$ at $\lambda = 2.61$ Å). Solid line represents a synthetic spectrum calculated from the atomic data given in Ref. 1 and Tables I—III. Synthetic spectrum has been least-squares fitted to the experimental data with respect to the ion and electron temperature and the relative abundance, $N_{Ti\,XX}/N_{Ti\,XXII}$, of the lithiumlike and heliumlike titanium charge states. The various components of the synthetic spectrum are separately shown in (b), (c), and (d). (b) Resonance, intercombination, and forbidden lines of heliumlike titanium, Ti XXI, corresponding to the transitions $1s^2\,{}^1S_0 - 1s2p\,{}^1P_1$ (w), $1s^2\,{}^1S_0 - 1s2p\,{}^3P_2$ (x), $1s^2\,{}^1S_0 - 1s2p\,{}^3P_1$ (y), and $1s^2\,{}^1S_0 - 1s2s\,{}^3S_1$ (z), respectively. Cross-hatched areas under x, y, and z represent the intensities which are predicted for electron impact excitation from ground state. Dotted areas under x, y, and z represent the intensities obtained from least-squares fits of Voigt functions to the experimental data. (c) Lithiumlike satellites due to transitions of the type $1s^2nl$-$1s2pnl$ with $n \geq 2$. The satellites are produced by dielectronic recombination of heliumlike titanium, Ti XXI. Their intensity relative to the intensity of the resonance line w is a function of the electron temperature alone. (d) Lithiumlike satellites from $1s^22s$-$1s2s2p$ transitions produced by collisional inner-shell excitation of lithiumlike titanium, Ti XX, and berylliumlike satellites, due to the transitions $1s^22snl$-$1s2s2pnl$, with $n \geq 3$ which are listed in Table IV. Berylliumlike satellites are produced by dielectronic recombination of Ti XX ions. Intensity ratio of the collisionally excited lithiumlike satellites and the resonance line w is proportional to the ratio $N_{Ti\,XX}/N_{Ti\,XXI}$ of the abundances of the lithiumlike and heliumlike charge states.

ison are shown in Fig. 3. The dotted curve in Fig. 3(a) represents experimental data which were recorded from 0.30 to 0.48 sec from an Ohmically heated plasma with $R = 2.55$ m, $a = 0.83$ m, $n_e(0) = 2.7 \times 10^{19}$ m^{-3}, and $T_e(0) = 1.8$ keV, during the period from 0.7 to 3.5 sec when I_p was constant at 1 MA. The solid curve in Fig. 3(a) represents a theoretically predicted spectrum. It was obtained by calculating Voigt profiles for the transition arrays given in Refs. 1 and 7 and in Tables V—VII of Sec. VII.

Figures 3(b)—3(d) show the contributions to the synthetic spectrum from the various excitation processes. Figure 3(b) shows the $1s^2\,{}^1S_0 - 1s\,2p\,{}^1P_1$ resonance line w, the $1s^2\,{}^1S_0 - 1s\,2p\,{}^3P_{1,2}$ intercombination lines y and x, and the $1s^2\,{}^1S_0 - 1s\,2s\,{}^3S_1$ forbidden line z which are produced mainly by electron impact excitation of Ti XXI ions from the heliumlike ground state: $1s^2\,{}^1S_0$. Figure 3(c) shows satellites due to transitions $1s^2nl\text{-}1s\,2lnl'$ with $n \geq 2$ resulting from dielectronic recombination of heliumlike titanium. Figure 3(d) shows satellites produced by both collisional inner-shell excitation of lithiumlike ions in the ground state, as well as berylliumlike satellite lines due to transitions $1s^2 2snl\text{-}1s\,2s\,2l'nl''$ with quantum number $n = 3$ and 4 resulting from dielectronic recombination of lithiumlike ions. The spectral features are identified by Gabriel's notation[28] and explained in Refs. 1 and 7.

The relative contributions of these spectral components to the synthetic spectrum have been determined from a least-squares fit to the experimental data. This fit was obtained in several steps.

As a first step, the part of the synthetic spectrum which consists of the Ti XXI resonance line w and the associated $1s^2nl\text{-}1s\,2pnl$ satellites with $n \geq 3$ has been fitted to the experimental data in the wavelength range from 2.6025 to 2.6160 Å. The arrows in Fig. 3(a) indicate the range of data points which were used for the fit and background determination. The $n \geq 3$ satellites are ascribed to dielectronic recombination of Ti XXI, and their intensities relative to the intensity of the resonance line w are a function of the electron temperature alone, given by expression (2.1) in Ref. 1. The spectrum is thus, theoretically, fully described by two important plasma parameters, the ion and the electron temperature, which determine the width of the resonance line and the satellite to resonance line ratios. A detailed comparison of theoretical predictions with experimental data obtained from the PDX has been given previously in Ref. 1, where we found very good agreement between theory and experiment if we applied minor corrections (of ~0.5 mÅ) to the theoretical wavelengths of some of the $n = 3$ satellite lines. These corrected wavelengths were used for the present calculations of the synthetic spectrum. No additional changes were made to describe the TFTR data. The ion and electron temperature values obtained from the fit to the data in Fig. 3 were $T_i = 1.12 \pm 0.07$ keV and $T_e = 1.33 \pm 0.06$ keV, respectively. We deduce from computation of radial profiles of the line emissivities, which are described in Sec. VIII, that these values correspond to the central ion and electron temperatures. Our values for the ion and electron temperatures agree with the central temperature results obtained by other diagnostics to within ten percent.[27]

As a second step, we use the inferred T_i and T_e values to calculate line profiles for the intercombination and forbidden lines (x, y, and z) and for the lithiumlike satellites ($1s^2nl\text{-}1s\,2pnl$ with $n = 2$) which result from the dielectronic recombination of heliumlike titanium, Ti XXI. The intensities of the intercombination lines and the forbidden line were calculated using the rate coefficients for direct excitation only from the $1s^2$ heliumlike ground state given in Table IV of our previous publication.[1] These theoretically predicted intensities are shown by the cross-hatched areas in Fig. 3(b). They are considerably smaller than the observed values. In order to obtain quantitative information on this deviation, the experimentally observed intensities of the intercombination and forbidden lines have been determined from a least-squares fit of Voigt functions to the data points. The intensity values obtained from this fit are represented by the dotted areas in Fig. 3(b). The observed intensity ratios, $I_x/I_w = 0.375$, $I_y/I_w = 0.5$, and $I_z/I_w = 0.5$, are larger by factors of 1.36, 2.49, and 5.3, respectively, than the values predicted for direct excitation. A detailed comparison of the experimental data with the current theoretical predictions which include contributions from additional excitation processes for the lines x, y, and z is given in Sec. V. The dielectronic contribution to the intensity of the $n = 2$ satellites (relative to the intensity of the resonance line w) is, again, a function of the electron temperature and was evaluated from expression (2.1) in Ref. 1. The results are shown in Fig. 3(c). We find good agreement for the satellites j and k which are entirely produced by dielectronic recombination.

As a third step, we calculated the intensity contributions to the lithiumlike $n = 2$ satellites from collisional inner-shell excitation of Ti XX ions and the contributions from berylliumlike $n \geq 3$ satellites, which are ascribed to dielectronic recombination of lithiumlike titanium. Although these satellites are produced by different atomic processes, they originate from lithiumlike ions, and their intensities are, therefore, proportional to the abundance of Ti XX. The contributions from collisional inner-shell excitation to the $n = 2$ satellites, such as q, a, r, m, s, and t, have been calculated from the excitation rate coefficients given in Table III of Ref. 1, and the dielectronic contribution from the $n \geq 3$ berylliumlike satellites has been determined from expression (7.1) in Sec. VII. The ratio of the satellite intensities to the intensity of the resonance line w is proportional to the ratio of the abundances of the lithiumlike and the heliumlike charge states, $N_{\text{Ti XX}}/N_{\text{Ti XXI}}$. The intensity contributions from these satellites, therefore, have been determined from a least-squares fit of the synthetic spectrum to the experimental data with respect to the parameters $N_{\text{Ti XX}}/N_{\text{Ti XXI}}$. From this fit we obtained for $N_{\text{Ti XX}}/N_{\text{Ti XXI}}$ the value 0.63 ± 0.04. The resulting spectral features are shown in Fig. 3(d). The contribution from the berylliumlike $n \geq 3$ satellites is represented by the cross-hatched area under q and r. This contribution is small compared with the contribution from lithiumlike satellites. The composite spectrum of the contributions shown in Figs. 3(c) and 3(d) represents the entire satellite spectrum in the spectral region from 2.6075 to 2.6360 Å and is in excellent agreement with the experimental observation. It is remarkable that this agreement is obtained

from a least-squares fit with respect to only three parameters, the ion and electron temperatures and the ratio of the lithiumlike and heliumlike abundance, $N_{\text{Ti xx}}/N_{\text{Ti xxi}}$. We conclude that the satellite spectrum is completely described by the two considered processes of dielectronic recombination and inner-shell excitation.
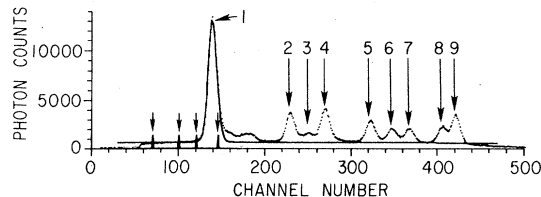

FIG. 4. Raw data used for wavelength determination of the main spectral features 1–9 described in Table I. The center of the prominent peaks has been determined from least-squares fits of single Voigt functions to the experimental data. Solid line shows the fit to the data points of peak 1. Arrows indicate the range of channels used for background determination and the Voigt-function fit.

IV. COMPARISON OF EXPERIMENTAL AND THEORETICAL WAVELENGTHS

Wavelength calculations for high-Z ions include relativistic and radiative corrections which are performed up to certain levels of accuracy.[29–33] In these calculations the wavelengths are approximated by a series of terms which have different dependencies on Z and different signs. It is difficult to predict on purely theoretical grounds whether a certain approximation is an adequate description of reality, and comparisons with experimental data are, therefore, important. Since our measurements are made with a resolving power of 25 000, they should be useful as a test of theoretical approximations.

In this section we compare our experimental results with the calculations of Bely-Dubau et al.[1] and Safronova et al.[7] which include relativistic and radiative corrections up to third order in the fine-structure constant α. The expected accuracy of the computed wavelengths is better than 1 mÅ. For these comparisons we determine the center positions of the main spectral features from least-squares fits of single Voigt functions, as shown for peak 1 in Fig. 4. The Voigt fit is done over the region indicated by the two rightmost arrows near peak 1. The two leftmost arrows mark the region over which a flat background subtraction is determined. The channel numbers obtained for the center positions are listed in Table I. From these channel numbers we then calculate the wavelengths from the dispersion function of the spectrometer using the theoretical value[7] of 2.6097 Å for line w as a

reference wavelength. The experimental values obtained in this way are shown in the Table I and compared with theoretical wavelengths of Bely-Dubau et al.[1] and Safronova et al.[7] Some of the observed satellite features can be ascribed to several lines which are listed in Table I with their line strengths. We infer from Table I that the experimental and theoretical wavelengths for the lines w, x, y, z and the $n=2$ satellites agree to within 0.5 mÅ, which also corresponds to the deviations between the two sets of theoretical predictions.

On the other hand, the observed main spectral features can be blended with unresolved higher-order lithiumlike satellites corresponding to a spectator electron in level $n \geq 3$. These satellites can cause significant wavelength shifts at low electron temperature and especially can affect the apparent resonance line w, which was used as a reference. To estimate these effects, we have done a least-squares Voigt-function fit to a synthetic spectrum consisting of a resonance line w and $n \geq 3$ dielectronic satellites, as illustrated in Fig. 5. Figures 5(a) and 5(b) show the resonance line (solid line) and the composite spectrum

TABLE I. Experimental wavelengths and theoretical calculations for the resonance, intercombination, and forbidden lines of Ti XXI, and associated satellite lines due to transitions $1s^2nl$-$1s2l'nl''$ with $n=2$. Wavelengths are in Å. Satellite line strengths $F_2(sf)$ are in units of 10^{13} s^{-1}.

Peak	Channel No.	Key	Transition	λ_{expt}	λ_{theor}[b]	$F_2(sf)$[b]	λ_{theor}[c]	$F_2(sf)$[c]
1	138.97	w	$1s^2\,{}^1S_0 - 1s2p\,{}^1P_1$	2.6097[a]	2.6099		2.6097	
2	228.78	x	$1s^2\,{}^1S_0 - 1s2p\,{}^3P_2$	2.6184	2.6186		2.6184	
		m	$1s^2 2p\,{}^2P_{3/2} - 1s2p^2\,{}^2S_{1/2}$		2.6192	3.705	2.6195	4.380
3	249.96	s	$1s^2 2s\,{}^2S_{1/2} - 1s2s2p\,{}^2P_{3/2}$	2.6205	2.6195	2.795	2.6197	1.510
		t	$1s^2 2s\,{}^2S_{1/2} - 1s2s2p\,{}^2P_{1/2}$		2.6205	7.775	2.6205	7.770
4	268.90	y	$1s^2\,{}^1S_0 - 1s2p\,{}^3P_1$	2.6223	2.6226		2.6221	
5	321.52	q	$1s^2 2s\,{}^2S_{1/2} - 1s2s2p\,{}^2P_{3/2}$	2.6272	2.6270	0.409	2.6272	0.107
		a	$1s^2 2p\,{}^2P_{3/2} - 1s2p^2\,{}^2P_{3/2}$		2.6293	7.608	2.6296	9.990
6	346.65	r	$1s^2 2s\,{}^2S_{1/2} - 1s2s2p\,{}^2P_{1/2}$	2.6295	2.6297	4.288	2.6295	3.740
		d	$1s^2 2p\,{}^2P_{1/2} - 1s2p^2\,{}^2P_{1/2}$		2.6291	0.066	2.6299	0.074
7	366.34	k	$1s^2 2p\,{}^2P_{1/2} - 1s2p^2\,{}^2D_{3/2}$	2.6313	2.6310	28.090	2.6314	30.600
		c	$1s^2 2p\,{}^2P_{3/2} - 1s2p^2\,{}^2P_{1/2}$		2.6338	0.022	2.6342	0.025
8	404.86	j	$1s^2 2p\,{}^2P_{3/2} - 1s2p^2\,{}^2D_{5/2}$	2.6348	2.6346	35.280	2.6348	42.200
		l	$1s^2 2p\,{}^2P_{3/2} - 1s2p^2\,{}^2D_{3/2}$		2.6360	1.004	2.6356	1.410
9	420.07	z	$1s^2\,{}^1S_0 - 1s2s\,{}^3S_1$	2.6362	2.6364		2.6362	

[a]The experimental wavelengths are normalized to the theoretical value of 2.6097 Å for the $1s^2\,{}^1S_0 - 1s2p\,{}^1P_1$ transition.
[b]Reference 1.
[c]Reference 7.

of w plus the $n \geq 3$ satellites (dashed line) for electron temperatures of 0.7 and 1.4 keV, respectively, and a fixed ion temperature of 2 keV. The channel numbers correspond to the wavelength dispersion of the spectrometer, so that the synthetic spectrum in Fig. 5 can be compared directly with the raw data spectrum shown in Fig. 4. The center position of the apparent resonance line was determined from a single-Voigt-function fit to the composite spectrum within the fitting limits indicated by the two arrows at channel numbers 120 and 145. The same fitting limits were used in Fig. 4. It can be seen that the "dielectronic red shift" of the apparent resonance line with respect to the true resonance line decreases with increasing electron temperature as the contribution from the $n \geq 3$ satellites decreases. The ion temperature values obtained from the single-Voigt-function fits in Figs. 5(a) and 5(b) are 2.41 and 2.11 keV, indicating that the true value of 2 keV is approached with increasing electron temperature.

The dielectronic red shift depends not only on electron temperature but also on the range of fitting limits and the ion temperature. These dependences are shown in Fig. 6. The solid curves were obtained for the fit limits shown in Fig. 5 (channels 120–145). The dashed curve was obtained using the fit limits from channel 120 to channel 150. The curves are labeled by the ion temperature values which were assumed for calculation of the synthetic spectrum. The solid curves are well approached by the expression

$$\Delta\lambda = \frac{2.75 \times 10^{-5} + 0.8 \times 10^{-5} T_i}{T_e} \exp(0.96/T_e) , \qquad (4.1)$$

where $\Delta\lambda$ is the dielectronic red shift of the apparent resonance line in Å, and T_i and T_e are the ion and electron temperatures in keV. For ion and electron temperatures

FIG. 6. Wavelength shift $\Delta\lambda$ of the apparent and true resonance line as a function of the electron temperature. Results have been derived from least-squares fits of single Voigt functions to synthetic spectra (as shown in Fig. 5) for a set of ion temperature values. Results presented by the solid curves and the dashed curve were obtained for different choices of fitting limits: channels 120–145 and channels 120–149, respectively.
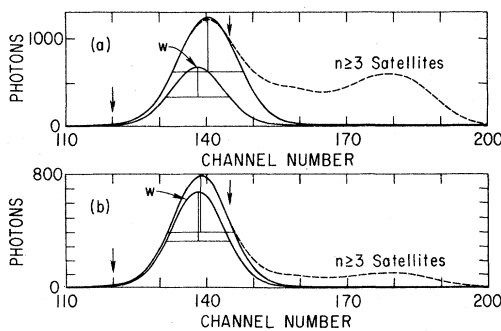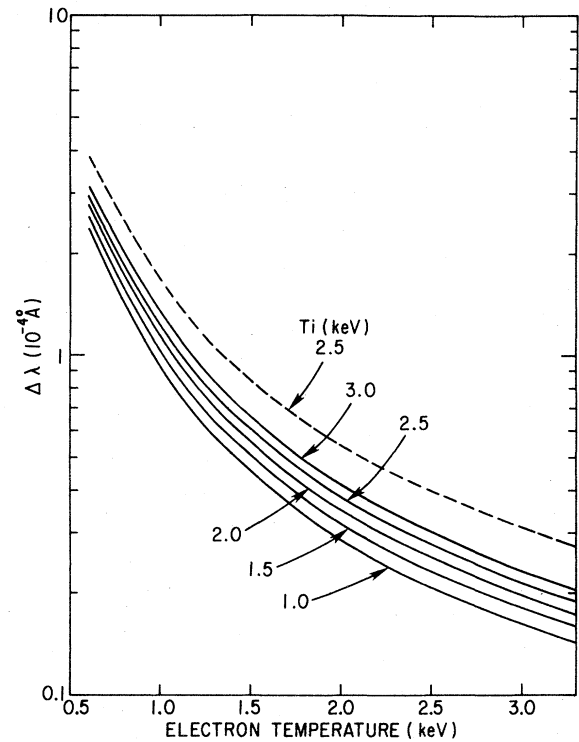

FIG. 5. Illustration of the line shift between the apparent and true resonance line due to unresolved dielectronic satellites. Dashed curves in (a) and (b) represent synthetic spectra of the resonance line w and the satellite transitions $1s^2 nl - 1s\, 2pnl$ with $n \geq 3$ for electron temperatures of 0.7 and 1.4 keV, respectively, and an ion temperature of 2 keV. Channel numbers correspond to the wavelength dispersion of the spectrometer. Solid lines represent the true resonance line w and a least-squares fit of a single Voigt function to the composite spectrum. The fit has been performed to the part of the synthetic spectrum shown in the channels from 120 to 145. This range of channels was also used for the fit shown in Fig. 4.

of 2 keV (corresponding to the parameters of the spectrum shown in Fig. 4 which was used for evaluation of the wavelength values given in Table I), the red shift of the apparent resonance line is 0.34 mÅ. Since this value is smaller than the uncertainties of the theoretical data given in Table I, it is acceptable for the present comparison of theoretical and experimental wavelengths to use the center position of the *apparent* resonance line as a reference. However, for comparison with more-precise calculations, one should use a reference, for example, the intercombination line y, which is much less contaminated by satellites (see Fig. 3). A comparison of our data with more-detailed wavelength calculations which include quantum electrodynamic effects and relativistic corrections to orders of α higher than 3 will be presented in a separate paper. Dielectronic red shifts of the apparent resonance line comparable to those shown in Fig. 6 have been observed experimentally and will be discussed in Sec. VIII. These dielectronic shifts must be taken into account as a correction for Doppler-shift measurements of the plasma rotation velocity during the injection of neutral hydrogen beams.

V. INTENSITY RATIOS OF THE HELIUMLIKE
LINES: x, y, z, and w

Deviations of the intensity ratios, I_x/I_w, I_y/I_w, and I_z/I_w, from the values predicted for direct excitation, such as shown in Fig. 3(b), have been observed previously in Fe XXV spectra, obtained from the PLT (Refs. 17 and 18) and other experiments.[3,5,9] Attempting to resolve these discrepancies, calculations[34-38] have been performed which include three additional processes for the population of the upper levels $1s2s\,^3S_1$ and $1s2p\,^3P_{1,2}$ of the lines z, y, and x: (1) electron impact excitation from the $1s^2\,^1S_0$ heliumlike ground state to levels with $n \geq 3$ followed by cascading, (2) recombination of hydrogenlike ions followed by cascading, and (3) inner-shell ionization of lithiumlike ions $(1s^2 2s\,^2S_{1/2}+e \rightarrow 1s2s\,^3S_1+e'+e'')$. These calculations have been in reasonable agreement with solar corona observations of O VII and Ne IX,[39] solar flare spectra of Ca XIX,[3] and spectra of C V, S XV, Cl XVI, and Ar XVII from tokamak plasmas[5,6,40-42] where a large fraction of the observed line intensities has been ascribed to the second process. However, they fail to describe the spectra of high-Z heliumlike ions, e.g., Ti XXI and Fe XXV, obtained from the PLT and TFTR tokamaks. We note that there are significant differences between the spectra of heliumlike ions with low atomic number ($Z < 20$) and the spectra of Ti XXI and Fe XXV.

(1) The relative intensities of the resonance, intercombination, and forbidden lines of Ti XXI and Fe XXV are less sensitive to the electron density than the line intensities of low-Z heliumlike ions, due to the fact that the probabilities for transitions $1s2p\,^3P_{1,2}-1s^2\,^1S_0$ and $1s2s\,^3S_1-1s^2\,^1S_0$ by radiation scale like Z^9, Z^8, and Z^{10}, respectively.[21,43] The intensity ratios I_x/I_w, I_y/I_w, and I_z/I_w of the Ti XXI lines are dependent on the electron density at densities above a critical value[28] $N_e^* \approx 1 \times 10^{15}$ cm^{-3}, which is much larger than the central density of TFTR plasmas. Density effects, therefore, can be neglected for the observed Ti XXI lines. This is different for spectra of C V, S XV, Ce XVI, and Ar XVII (Refs. 5, 6, and 40–42) obtained from tokamak plasmas where density effects should be important.[28]

(2) Since the wavelength separation of the spectral features also increases with increasing Z, the lines x, y, and z are well-resolved from dielectronic satellites in spectra of Ti XXI and Fe XXV, and their intensities can be determined with good experimental accuracy. For $Z \leq 20$, however, the forbidden line z is unresolved from the strong dielectronic satellite j. Thus the intensity of line z has additional uncertainty resulting from corrections for dielectronic recombination.

(3) Hydrogenlike ions of low-Z elements (e.g., Ar XVIII) can easily be produced in present-day tokamaks, where central electron temperatures of 1–2 keV are typical. Thus, contributions to lines x, y, and z due to recombination of hydrogenlike ions followed by cascading can be important. On the other hand, electron temperatures well in excess of 2 keV [see Figs. 1(b) and 2] are required to produce significant concentrations of hydrogenlike titanium and iron, i.e., Ti XXII and Fe XXVI. Thus, this contribution is negligible in the present case. In particular, large values of I_x, I_y, and I_z were observed at the begin-

ning of TFTR discharges, when the electron temperature was below 1 keV and hydrogenlike titanium was not present.

The Fe XXV spectra from PLT have been compared with recent theoretical predictions by Pradhan. He concluded that other atomic processes, in addition to recombination, should be included to fully compare the PLT observations with the model described in Ref. 42.

An illustration of the strong variation of the relative intensity of x, y, z, and w with T_e is shown in Fig. 7, which presents a time sequence of spectra from the early phases of a discharge. The intensities of x, y, and z with respect to w are very strong at the beginning of the discharge and then decrease with increasing electron temperature, as does the intensity of q relative to w (which is proportional to the abundance of lithiumlike relative to heliumlike titanium). Figure 8 presents observed line ratios versus T_e for a large range of discharge parameters. Also shown are theoretical predictions for these ratios assuming direct excitation to $n = 2$ (solid line) and direct excitation to $n > 2$ including radiative cascades and collisional resonances (dashed line). These theoretical predictions represent the excitation of Ti XXI ions from the ground state, and they are expected to describe the data in the electron temperature range from 1.2 to 2 keV where the abundances of hydrogenlike and lithiumlike titanium and, consequently, the processes of line excitation by recombination and inner-shell ionization are negligible. We infer from Fig. 8 that the theoretical predictions are in good general agreement with the experimental data in the considered range of electron temperatures above 1.2 keV, even though we also observe some deviations. The predicted intensity ratios of I_x/I_w and I_y/I_w are somewhat smaller than the observed values, and the predicted contributions from impact excitation including cascades and resonances evidently overestimate the experimental values of I_z/I_w. This suggests that the theory is basically correct except for the predictions of the relative population of the triplet levels.
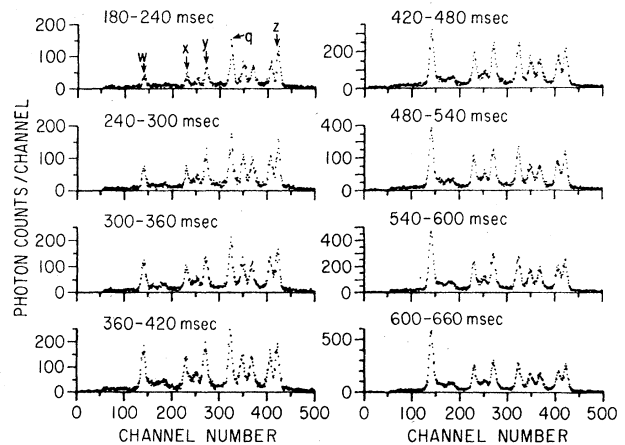

FIG. 7. Spectra recorded from an Ohmically heated plasma of a TFTR discharge during consecutive time intervals of 60 ms. Intensities of the intercombination lines x, y, the forbidden line z, and the lithiumlike line q relative to the intensity of the resonance line w decrease as the electron temperature rises with time during a TFTR discharge.
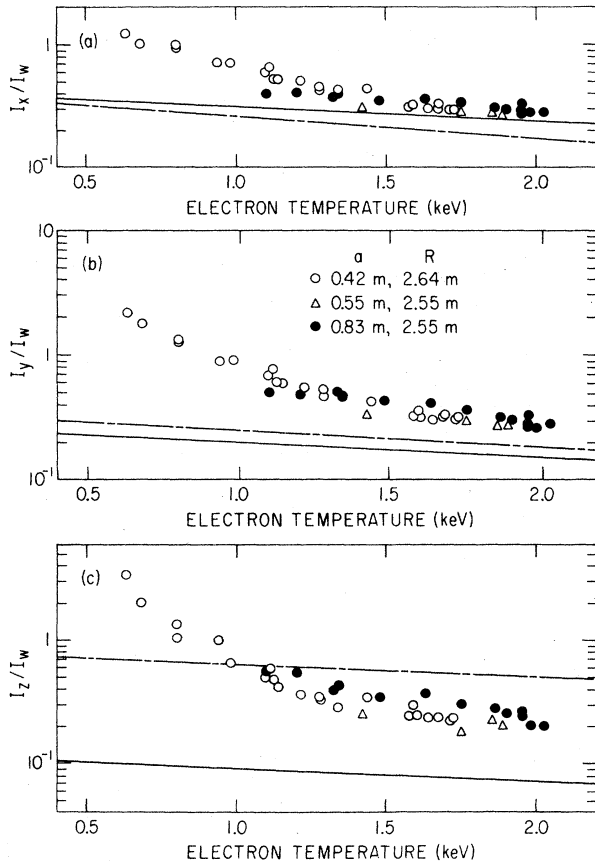
FIG. 8. Experimental values of the intensity ratios I_x/I_w, I_y/I_w, and I_z/I_w vs the central electron temperature. Data have been obtained from Ohmic discharges with different minor and major radii a and R, respectively. Also shown are the intensity ratios predicted for direct electron impact excitation from the ground state (solid lines) and electron impact excitation to levels $n \geq 2$ including cascading (dashed lines).

Therefore, we have considered the sum of the intensity ratios, $G = (I_x + I_y + I_z)/I_w$, which is independent of the relative population of the upper triplet states. Figure 9 represents a comparison between the predictions and ex-
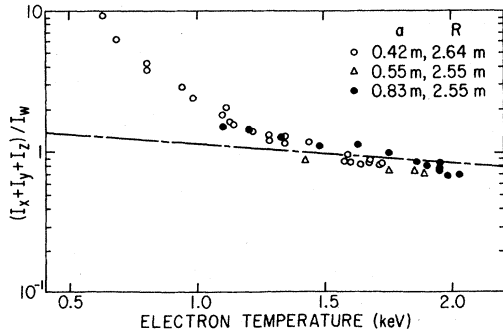

FIG. 9. Experimental values and predictions for the total intensity of the intercombination and forbidden lines relative to the intensity of the resonance line, $G = (I_x + I_y + I_z)/I_w$, vs electron temperature. Theoretical predictions shown by the dashed curve include the contributions from electron impact excitation and cascading Ti XXI.

perimental results. Theory and experiment are evidently in very good agreement for the range of electron temperatures from 1.2 to 2 keV. On the other hand, there are large discrepancies by as much as 1 order of magnitude at electron temperatures < 1.2 keV. These discrepancies cannot be explained by the contribution from inner-shell ionization of Ti XX. We have calculated this contribution using the experimental values of $N_{\mathrm{Ti\,XX}}/N_{\mathrm{Ti\,XXI}}$ deduced from a fit of the satellites q, r, m, s, and t as described in Sec. III, and the theoretical ionization rate coefficients given in Table IV of Sec. VI. From this calculation we obtain values of $I_z/I_w = 0.1$ at $T_e = 0.6$ keV and $I_z/I_w = 0.03$ at 2 keV for the contribution from inner-shell ionization to the forbidden line. These values are much too small to account for the discrepancies. Enhancement of the observed line intensities of x, y, and z due to the presence of unresolved lithiumlike and beryl-liumlike dielectronic satellites obviously can be excluded according to theoretical predictions (see Fig. 3).

An inspection of the data indicates that the ratios I_x/I_w, I_y/I_w, and I_z/I_w have a variation with electron temperature similar to that of $N_{\mathrm{Ti\,XX}}/N_{\mathrm{Ti\,XXI}}$, which is shown in Fig. 10. This suggests that the enhancement of observed intensities of these lines relative to theory is likely related to the presence of lithiumlike titanium, which is more abundant at low T_e (see Fig. 10).

Analyzing our data we find indeed a quantitative correlation between measured values of $G = (I_z + I_y + I_z)/I_w$ and the observed $N_{\mathrm{Ti\,XX}}/N_{\mathrm{Ti\,XXI}}$ ratio. Figure 11 shows the difference between the experimental and theoretical values of G as a function of the measured lithiumlike to heliumlike titanium ratio. The straight line given by the equation

$$G_{\mathrm{expt}} - G_{\mathrm{theor}} = -0.55 \pm 0.19$$

$$+ (1.44 \pm 0.15) N_{\mathrm{Ti\,XX}}/N_{\mathrm{Ti\,XXI}} \qquad (5.1)$$
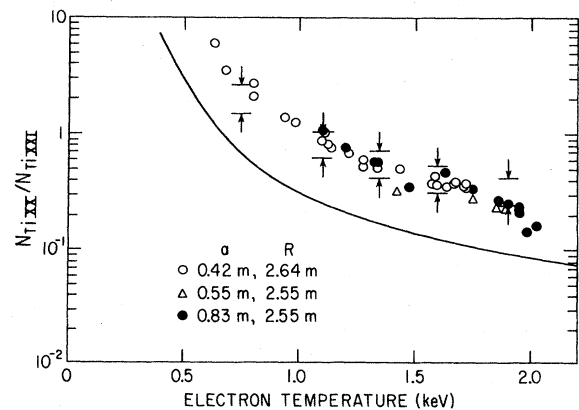

FIG. 10. Relative abundances $N_{\mathrm{Ti\,XX}}/N_{\mathrm{Ti\,XXI}}$ of lithiumlike and heliumlike titanium vs electron temperature. Values for the ratio of these abundances have been obtained from the detailed comparison of the theoretical predictions for the collisionally excited lithiumlike satellites with the experimental data as illustrated in Fig. 3(d). Solid curve represents theoretical values expected for coronal equilibrium, while the bracketed points are derived from plasma model calculations (see text).
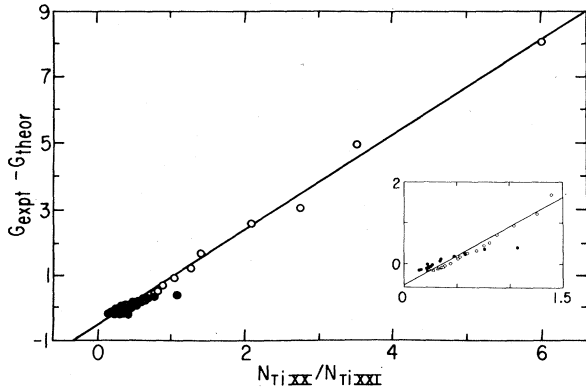
FIG. 11. Difference of the observed and predicted values of $G = (I_x + I_y + I_z)/I_w$ vs the experimental values of $N_{\text{Ti\,XX}}/N_{\text{Ti\,XXI}}$ shown in Fig. 10.

has been obtained from a least-squares fit to the data. These results again strongly imply that the predominant contribution to these lines at low T_e is from lithiumlike ions.

We have considered several mechanisms in search of an explanation for this contribution. One mechanism has been suggested by Kim.[44] It is a two-step process consisting of excitation of a lithiumlike ion from the ground state to the metastable level $1s2s2p\,^4P_{5/2}$, followed by collisional ionization of one of the L-shell electrons. Removal of the $2p$ electron would produce the $1s2s\,^3S_1$ state and contribute to line z, and removal of the $2s$ electron would result in a $1s2p\,^3P_{1,2}$ state, which would contribute to lines x or y. Since this mechanism produces only triplet states, it could explain the enhancement of lines x, y, and z relative to w. The excitation of this metastable level is very strong (see Table III in Ref. 1). However, the lifetime of this $^4P_{5/2}$ level due to $M2$ radiation and autoionization to the heliumlike ground state is only 0.2 ns,[45] which is orders of magnitude smaller than the collisional ionization time. This process is unlikely in tokamak plasmas.

## VI. THEORY FOR THE HELIUMLIKE LINES:
w, x, y, and z

In this section we present theoretical results on rate coefficients for population of the upper levels $1s2p\,^1P_1$, $^3P_2, ^3P_1$ and $1s2s\,^3S_1$ of the lines w, x, y, and z by the previously mentioned processes (see Sec. V) of electron impact excitation, recombination, and inner-shell ionization. The line emissivities are then obtained by solving a set of equations:

$$\epsilon = N_e N_{\text{He}} \left[C + \alpha \frac{N_{\text{H}}}{N_{\text{He}}} + S \frac{N_{\text{Li}}}{N_{\text{He}}} \right] , \tag{6.1}$$

where N_e, N_{H}, N_{He}, and N_{Li} are the densities of the free electrons and the H-like, He-like, and Li-like ions, respectively. C, α, and S are the rate coefficients for electron impact excitation, recombination, and inner-shell ioniza-

tion. The direct excitation rates for the heliumlike lines have been calculated in Ref. 1. These results did not take into account the effect of cascades and resonances. Cascades are important for these levels, especially for the triplet system. Previous results show that cascades increase the direct excitation rate for $1s2s\,^3S_1$ by a factor of 3.5 at 3×10^7 K (2.59 keV) for Fe XXV (Ref. 38) and by a factor of 4 at 1×10^7 K (0.86 keV) for Ca XIX.[3] The effect of resonances is less important than radiative cascades. However, recent calculations by Faucher and Dubau[46] show that resonances increase the direct excitation rate for the Fe XXV $1s2s\,^3S_1$ level by a factor of 1.2 at 3×10^7 K. It is thus interesting to take this process into account for the population of the heliumlike excited levels. For the highly ionized atoms, the resonances due to the autoionizing levels $1s3l'nl$ are more efficient than those due to the autoionizing levels $1s2l'nl$ (by a factor of 4.5 for the Fe XXV $1s2s\,^3S_1$ level at 3×10^7 K).

In the present work the method for calculating the excitation of He-like levels through cascades follows closely that described for Fe XXV by Bely-Dubau *et al.*[38] The collision strengths of Sampson *et al.*[47] were used for excitation from $1s^2\,^1S_0$ to $1snl$ for $3 \leq n \leq 5$. On the other hand, the contribution of the $1s3l3l'$ autoionizing levels to the excitation rates of the He-like lines was calculated using the method described by Faucher and Dubau. The corresponding excitation rates C (cm^3 s^{-1}) are obtained from the following electron-atom collision process:

$$1s^2\,^1S + e \rightarrow 1s3l'3l\ ^{2S'+1}L_J \rightarrow 1s2l''\ ^{2S'+1}L_{J'} + e' . \tag{6.2}$$
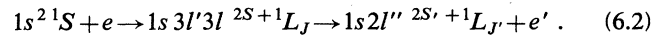
The same values for these excitation rates were obtained from the corresponding Fe XXV results using the asymptotic Z dependence,[48]

$$Z^3 C(T_e) + f(T_e/Z^2) . \tag{6.3}$$

Thus, the contribution of all the autoionizing levels to the He-like Ti XXI excitation rate was evaluated by extrapolation from Fe XXV results for the $1s3l'nl$ autoionizing resonances by Faucher and Dubau[46] and for the $1s2l'nl$ autoionizing resonances by Steenman-Clark and Faucher.[49]

Table II shows the effective excitation rate coefficients C for the He-like Ti XXI levels including cascade contributions and resonance effects due to the $1snln'l'$ autoionizing states with $n = 2, 3$. The effect of cascades and resonances is shown in Table III for the temperature of 2×10^7 K (1.72 keV), where column A represents the direct excitation rates given in Ref. 1.

The excited levels of Ti XXI are also populated by recombination processes from Ti XXII. Although this contribution is negligible for our observations, we include the theoretical calculations for completeness. Only radiative and dielectronic recombination have been considered. The contributions of the Ti XXII excited levels are negligible for low-density plasmas. Charge-exchange recombination of the H-like ionization stage can be important in tokamak plasmas, but this process has not been considered in this work. To evaluate the radiative recombination rates, hydrogenic calculations were used following the method described by Bely-Dubau *et al.*[38] The dielectronic recombination rates were taken from Ref. 2, the autoionizing states being grouped to give the total rates for the

TABLE II. Effective excitation rate coefficients $(cm^3 s^{-1})$ of spectral lines produced from Ti XXI, including radiative cascades and collisional resonances. Numbers enclosed in parentheses signify powers of 10.

T_e $(10^6$ K)	$C(z)$	$C(y)$	$C(x)$	$C(w)$
4	1.19(−17)	5.01(−18)	5.25(−18)	1.46(−17)
6	9.24(−16)	3.85(−16)	4.02(−16)	1.26(−15)
8	7.99(−15)	3.21(−15)	3.34(−15)	1.15(−14)
10	2.84(−14)	1.11(−14)	1.15(−14)	4.29(−14)
12	6.42(−14)	2.48(−14)	2.53(−14)	1.03(−13)
15	1.46(−13)	5.43(−14)	5.43(−14)	2.47(−13)
17	2.12(−13)	7.76(−14)	7.64(−14)	3.72(−13)
20	3.17(−13)	1.14(−13)	1.10(−13)	5.89(−13)
25	4.88(−13)	1.71(−13)	1.60(−13)	9.92(−13)
30	6.42(−13)	2.20(−13)	1.99(−13)	1.40(−12)
40	8.65(−13)	2.89(−13)	2.46(−13)	2.17(−12)

production of $1snl$ levels.

Finally, the $1s2s\,^3S_1$ level of Ti XXI can be populated by removing an inner-shell electron from the $1s^22s\,^2S_{1/2}$ ground state of Ti XX. The process is important for line z, and its contribution was calculated using the Lotz formula.[50] The effective recombination rates α and the ionizing rate coefficient S for the line z are given in Table IV.

VII. THEORY FOR THE BERYLLIUMLIKE SATELLITES

The calculations in Ref. 1 were done for all the satellites of the heliumlike Ti XXI lines corresponding to the transitions $1s^2nl$-$1s2l'nl''$ with $n=2$, 3, and 4. Here the satellite lines $1s^22lnl'$-$1s2p2l''nl'''$ with $n=2$, 3, and 4 are considered. These lines belong to the berylliumlike charge state Ti XIX and some of them are observed in the same spectral range (2.622–2.634 Å) where they are blended with the Ti XX lines. They are formed by dielectronic recombination from the Li-like ion Ti XX. The emissivity for these lines is obtained from the expression[16]

$$\epsilon_d = N_e N_{Z+1} F_1^*(s,T_e) F_2^*(sf) , \qquad (7.1)$$

where

$$F_1^*(s,T_e) = \frac{1}{2}\left[\frac{2\pi\hbar^2}{mkT_e}\right]^{3/2} \exp\left[\frac{-E_{si}}{kT_e}\right] , \qquad (7.2)$$

$$F_2^*(sf) = \frac{g_s}{g_i}\frac{A_a^{si}A_r^{sf}}{\sum_j A_a^{sj} + \sum_{f'} A_r^{sf'}} . \qquad (7.3)$$

TABLE III. Excitation rate coefficients $(cm^3 s^{-1})$ for Ti XXI at $T_e = 2 \times 10^7$ K (1.72 keV) showing A, direct excitation only; B, including cascades and resonances.

	A	B
$1s2s\,^3S_1$	4.53(−14)	3.17(−13)
$1s2p\,^3P_0$	2.56(−14)	0
$1s2p\,^3P_1$	9.64(−14)	1.14(−13)
$1s2p\,^3P_2$	1.28(−13)	1.10(−13)
$1s2p\,^1P_1$	5.54(−13)	5.89(−13)

N_{Z+1} is the density of the recombining ion, $Z+1$ times ionized; N_e and T_e are the electron density and temperature; m, k, and $\hbar$ are, respectively, the electron mass, the Boltzmann constant, and the Planck constant; g_s is the statistical weight of the upper level s of the line (sf), and g_i is the statistical weight of the ground state of the recombining ion; A_r and A_a are the radiative and autoionization transition probabilities. The sum over f' extends over all levels of the Z ion lower than s. The sum over j extends over all levels of the $Z+1$ ion which can be populated by autoionization of s; E_{si} is the energy of the free electron after autoionization from the levels s to i. For the three different shells $n=2$, 3, and 4, the average energies used are, respectively, $E_{si}(n=2)=250$ Ry, $E_{si}(n=3)=307$ Ry, and $E_{si}(n=4)=321$ Ry. The wavelengths λ and the line factors $F_2^*(sf)$ are given in Tables V–VII. For $n=2$ satellite lines all the necessary parameters are given in Table V in order to show their respective contributions in $F_2^*(sf)$. These parameters are calculated using the program SUPERSTRUCTURE (Ref. 51) and the program AUTOLSJ.[16] SUPERSTRUCTURE uses a parametric Thomas-Fermi-Dirac potential $V(\lambda_l,r)$ and a multiconfiguration basis. The values of λ_l for $l=0,1,2$ of the parametric potential are obtained using a minimization procedure based upon the energies of some selected Ti XIX terms, as it is generally done ($\lambda_s = 1.885$, $\lambda_p = \lambda_d = 1.587$). However, to obtain a better convergence for the $n>2$ satellite lines, we also used the orbitals which were calculated in Ref. 1 for the three electron satellite lines. In order to keep the calculations manageable, two complementary sets of configurations were introduced. The sets contain the even (or the odd) configurations for the doubly excited levels and, in each case, all the singly excited configurations. In each set the configurations $1s2l2l'4l''$ were treated without taking account of the configurations $1s2l2l'3l''$ which do not interact significantly with them. Such a choice is valid because the different "Layzer" complexes for Ti XIX are well separated in energy.

Using first-order perturbation theory the AUTOLSJ program calculates interaction matrix elements between a bound $(N+1)$-electron system and an $(N+1)$-electron system which is composed of a bound N-electron system and a free electron. For each autoionizing level, all the

TABLE IV. Effective recombination rate coefficients from H-like $1s$ titanium and ionization rate coefficient S_z from Li-like $1s^2 2s$ titanium in units of $cm^3 s^{-1}$.

T_e (10^6 K)	α_w	α_x	α_y	α_z	S_z
4	9.85(−13)	1.19(−12)	1.01(−12)	2.07(−12)	2.40(−20)
6	6.94(−13)	8.30(−13)	7.04(−13)	1.52(−12)	1.26(−17)
8	5.52(−13)	6.42(−13)	5.44(−13)	1.22(−12)	2.98(−16)
10	4.76(−13)	5.28(−13)	4.44(−13)	1.03(−12)	2.02(−15)
12	4.31(−13)	4.51(−13)	3.77(−13)	9.01(−13)	7.34(−15)
15	3.91(−13)	3.75(−13)	3.10(−13)	7.68(−13)	2.69(−14)
17	3.73(−13)	3.39(−13)	2.79(−13)	7.04(−13)	4.99(−14)
20	3.50(−13)	2.97(−13)	2.42(−13)	6.29(−13)	1.01(−13)
25	3.17(−13)	2.48(−13)	2.00(−13)	5.38(−13)	2.24(−13)
30	2.88(−13)	2.13(−13)	1.70(−13)	4.72(−13)	3.85(−13)
40	2.39(−13)	1.64(−13)	1.30(−13)	3.78(−13)	7.66(−13)

possible interactions have been considered in order to calculate the autoionization probabilities A_a, which are included in the line factors $F_2^*(sf)$ in formula (7.3). A double difference correction of $\Delta\lambda = +0.0025$ Å was applied to all the Ti XIX lines for consistency with the data given in Ref. 1.

VIII. DIAGNOSTIC APPLICATIONS

The spectra of high-Z ions are of great interest for the diagnosis of central parameters in large tokamak plasmas.

The most important diagnostic applications are measurements of the central ion temperature and the central plasma rotation velocity from Doppler broadening of and Doppler shift of spectral lines. In the following paragraphs we present results on the central ion temperature and toroidal rotation velocity from Ohmic and neutral beam heated TFTR plasmas.

Figure 12 shows a time sequence of Ti XXI resonance line profiles which were observed from a discharge with additional heating by injection of neutral hydrogen during the time interval from 2.3 to 2.8 sec. The average energy of the injected atoms was 25 keV per nucleon, and the total injected beam power was 1.15 MW. The Ti XXI resonance line profiles clearly show a broadening and a wave-

TABLE V. Atomic data for the principal satellites of the Ti XX $1s^2 2s-1s 2s 2p$ line due to transitions $1s^2 2lnl'-1s 2l2l''nl'''$ with $n = 2$. Corrected wavelengths are in Å. Probabilities A_a^s and A_r^{sf} and the line factors $F_2^*(sf)$ are in units of 10^{13} s^{-1}.

Transition	λ (Å)	A_a^s	$\sum A_a$	A_r^{sf}	$F_2^*(sf)$
$1s^2 2p^2\,^3P_2 - 1s\,2s^2 2p\,^3P_2$	2.7115	6.441	1.867	0.374	0.313
$1s^2 2s\,2p\,^3P_2 - 1s\,2s 2p^2\,^5p_3$	2.6702	0.201	0.231	0.157	0.286
$1s^2 2s 2p\,^1P_1 - 1s\,2s 2p^2\,^1D_2$	2.6551	10.630	24.480	8.690	6.628
$1s^2 2s^2\,^1S_0 - 1s\,2s 2p^2\,^3P_1$	2.6550	6.261	18.300	0.780	0.373
$1s^2 2s 2p\,^3P_2 - 1s\,2s 2p^2\,^3D_1$	2.6516	5.448	7.102	5.432	1.333
$1s^2 2s 2p\,^1P_1 - 1s\,2s 2p^2\,^3P_2$	2.6514	3.864	20.300	3.007	1.224
$1s^2 2s 2p\,^3P_2 - 1s\,2s 2p^2\,^3D_2$	2.6510	11.420	13.190	0.784	0.747
$1s^2 2s 2p\,^3P_2 - 1s\,2s 2p^2\,^3D_3$	2.6499	14.310	16.400	11.440	20.580
$1s^2 2s 2p\,^3P_2 - 1s\,2s 2p^2\,^3P_1$	2.6497	9.055	11.610	5.698	2.489
$1s^2 2s 2p\,^3P_1 - 1s\,2s 2p^2\,^3D_1$	2.6480	5.448	7.102	1.549	0.380
$1s^2 2s 2p\,^3P_1 - 1s\,2s 2p^2\,^3D_2$	2.6475	11.420	13.190	15.950	15.180
$1s^2 2s 2p\,^3P_2 - 1s\,2s 2p^2\,^3P_2$	2.6475	3.266	5.884	27.160	6.291
$1s^2 2s 2p\,^3P_0 - 1s\,2s 2p^2\,^3D_1$	2.6466	5.448	7.102	19.210	4.714
$1s^2 2s 2p\,^3P_1 - 1s\,2s 2p^2\,^3P_1$	2.6461	9.056	11.610	13.740	6.002
$1s^2 2s 2p\,^3P_1 - 1s\,2s 2p^2\,^3P_2$	2.6439	3.226	5.884	1.659	0.384
$1s^2 2s 2p\,^1P_1 - 1s\,2s 2p^2\,^1S_0$	2.6433	5.744	20.090	11.780	1.067
$1s^2 2s^2\,^1S_0 - 1s\,2s^2 2p\,^1P_1$	2.6427	0.305	12.790	22.760	0.285
$1s^2 2s 2p\,^3P_2 - 1s\,2s 2p^2\,^3S_1$	2.6410	4.227	10.330	6.009	1.902
$1s^2 2s 2p\,^3P_1 - 1s\,2s 2p^2\,^3S_1$	2.6374	4.227	10.330	2.747	0.870
$1s^2 2s 2p\,^3P_2 - 1s\,2s 2p^2\,^1D_2$	2.6372	10.630	24.780	1.641	1.252
$1s^2 2s 2p\,^3P_2 - 1s\,2s 2p^2\,^3P_1$	2.6361	1.353	13.580	5.009	0.539

TABLE VI. Atomic data for the principal satellites of the Ti XX $1s^22s-1s2s2p$ line due to transitions $1s^22lnl'-1s2l2l''nl'''$ with $n=3$. Corrected wavelengths are in Å. Line factors $F_2(sf)$ are in units of 10^{13} s^{-1}.

Transition	λ (Å)	$F_2^*(sf)$
$1s^22s3p\,^3P_2-1s2s2p3p\,^3D_2$	2.6470	0.310
$1s^22p3s\,^3P_3-1s2s2p3p\,^3D_3$	2.6452	0.510
$1s^22p3s\,^1P_1-1s2s2p3p\,^3D_2$	2.6446	0.359
$1s^22s3p\,^1P_1-1s2p^23s\,^5P_1$	2.6352	0.257
$1s^22s3p\,^3P_2-1s2s2p3p\,^3D_2$	2.6351	0.610
$1s^22s3p\,^1P_1-1s2s2p3p\,^3D_2$	2.6348	0.819
$1s^22s3p\,^3P_1-1s2s2p3p\,^3D_2$	2.6334	0.396
$1s^22s3p\,^3P_2-1s2p^23p\,^5D_2$	2.6328	4.286
$1s^22s3d\,^3D_1-1s2p^23p\,^5D_2$	2.6325	0.452
$1s^22p3s\,^3P_1-1s2p^23s\,^3P_0$	2.6324	0.258
$1s^22p3p\,^1P_1-1s2s2p3p\,^1D_2$	2.6322	0.722
$1s^22s3s\,^1S_0-1s2s2p3s\,^3P_1$	2.6321	0.497
$1s^22s3d\,^3D_3-1s2s2p3d\,^3F_3$	2.6314	0.974
$1s^22s3d\,^3D_2-1s2s2p3d\,^3F_3$	2.6311	0.709
$1s^22s3p\,^1P_1-1s2s2p3p\,^3P_1$	2.6311	0.340
$1s^22s3p\,^3P_1-1s2s2p3p\,^1D_2$	2.6309	4.087
$1s^22s3d\,^1D_2-1s2s2p3d\,^1F_3$	2.6307	2.031
$1s^22s3d\,^3D_3-1s2s2p3d\,^3D_3$	2.6298	0.365
$1s^22s3d\,^3D_3-1s2s2p3d\,^3F_4$	2.6294	3.994
$1s^22s3d\,^3D_2-1s2s2p3d\,^3D_3$	2.6295	0.394
$1s^22s3p\,^3P_2-1s2s2p3p\,^3P_2$	2.6268	1.000
$1s^22s3p\,^1P_1-1s2s2p3p\,^3P_2$	2.6264	0.658
$1s^22s3p\,^3P_3-1s2s2p3p\,^3D_2$	2.6263	0.659
$1s^22s3p\,^3P_0-1s2s2p3p\,^3D_1$	2.6257	0.634
$1s^22s3p\,^3P_1-1s2s2p3p\,^3D_1$	2.6256	0.774
$1s^22s3s\,^1S_0-1s2s2p3s\,^1P_1$	2.6250	0.368

TABLE VII. Atomic data for the principal satellites of the Ti XX $1s^22s-1s2s2p$ line due to transitions $1s^22lnl'-1s2l2l''nl'''$ with $n=4$. Corrected wavelengths are in Å. Line factors $F_2^*(sf)$ are in units of 10^{13} s^{-1}.

| Transition	λ (Å)	$F_2^*(sf)$
$1s^22s4d\,^3D_3-1s2s2p4d\,^3F_4$	2.6428	0.120
$1s^22s4p\,^1P_1-1s2s2p4p\,^3D_2$	2.6317	0.526
$1s^22s4p\,^3P_2-1s2s2p4p\,^3D_2$	2.6314	0.727
$1s^22s4d\,^3D_2-1s2s2p4d\,^3F_2$	2.6309	0.229
$1s^22s4d\,^3D_1-1s2s2p4d\,^3F_2$	2.6309	0.352
$1s^22s4d\,^3D_3-1s2s2p4d\,^3F_3$	2.6303	0.597
$1s^22s4d\,^3D_2-1s2s2p4d\,^3F_3$	2.6302	0.396
$1s^22p4p\,^3P_2-1s2s2p4p\,^3D_3$	2.6291	2.311
$1s^22p4p\,^1P_1-1s2s2p4p\,^3P_2$	2.6289	0.849
$1s^22s4s\,^3S_0-1s2s2p4s\,^1P_1$	2.6289	0.202
$1s^22p4p\,^3P_1-1s2s2p4p\,^1D_2$	2.6287	1.707
$1s^22p4p\,^3P_2-1s2s2p4p\,^2P_2$	2.6287	0.635
$1s^22p4p\,^3D_3-1s2s2p4p\,^3F_4$	2.6287	2.638
$1s^22p4p\,^3D_2-1s2s2p4p\,^3D_3$	2.6281	0.344
$1s^22p4p\,^1D_2-1s2s2p4p\,^1F_3$	2.6281	1.973
$1s^22s4d\,^1D_2-1s2s2p4s\,^1P_1$	2.6279	0.144
$1s^22s4f\,^3F_4-1s2s2p4f\,^3G_5$	2.6269	0.245
$1s^22s4f\,^3F_2-1s2s3p24f\,^3D_1$	2.6266	0.160
$1s^22p4p\,^3P_1-1s2s2p4p\,^3D_1$	2.6223	0.198
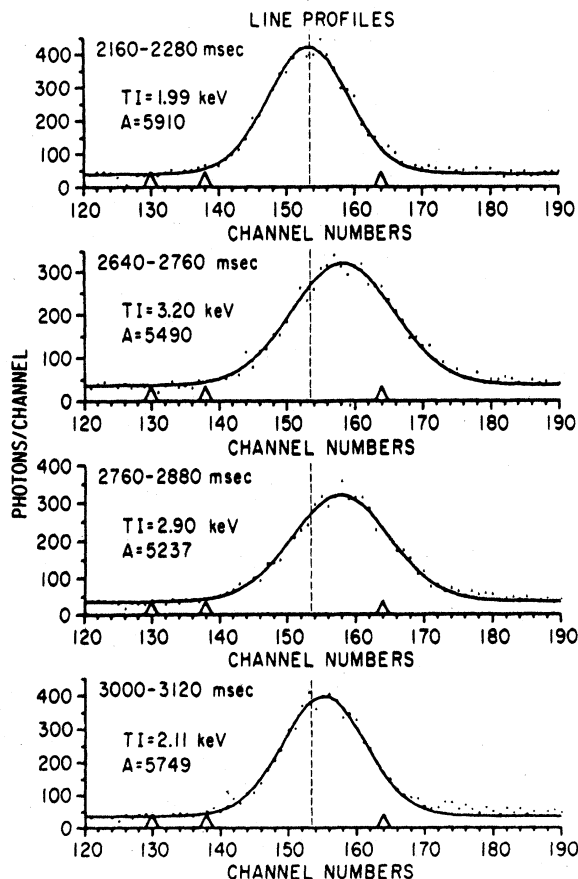
LINE PROFILES

FIG. 12. Ti XXI $K\alpha$ line profiles before, during, and after the injection of a neutral hydrogen beam of 25 keV energy and 1.15 MW total power into a TFTR discharge with a central electron density of 2×10^{13} cm^{-3}.

length shift due to the Doppler effect. The broadening is due to the thermal motion of the titanium ions and the shift results from a net toroidal rotation of the plasma produced by the neutral beam injection.

Figures 13(a) and 13(b) show the deduced ion temperature and the shift of the line center position as a function of time. The ion temperature increases from the value of 2.0 keV which is obtained during the Ohmic heating phase to 3.2 keV during the period of neutral beam injection. Figure 13(b) presents the center position of the line as a function of time. The scales on the ordinate give the observed wavelength shift and the deduced toroidal rotation velocity. Since the spectrometer line of sight makes an angle of 68° relative to the plasma toroidal direction, the observed wavelength shift measures a fraction of 37% of the actual toroidal rotation. As a reference for rotation velocity, we use the center position of the line immediately before injection, during the Ohmic heating phase.

The maximum toroidal rotation velocity is 1.5×10^7 cm/s, which is in reasonable agreement with the rotation velocity expected from the input torque to the plasma
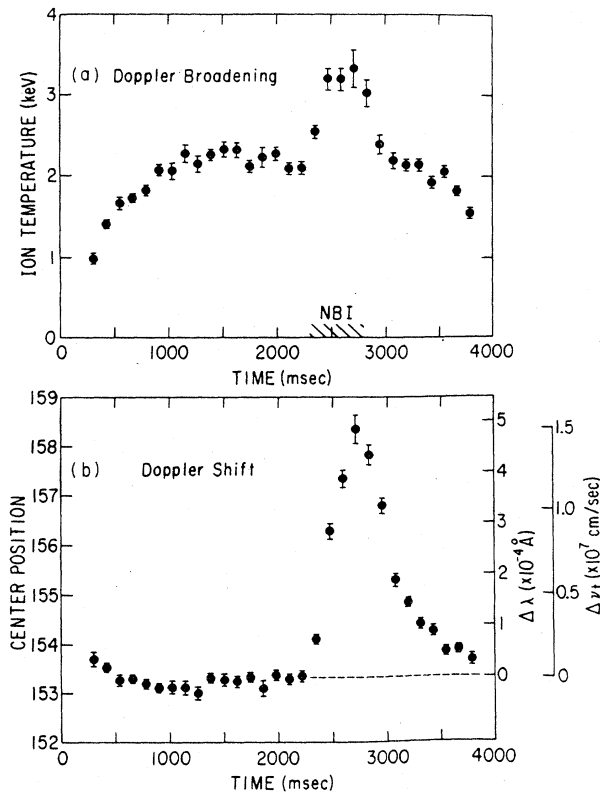
FIG. 13. Ion temperature results and toroidal plasma rotation velocities from measurements of the Doppler width and Doppler shift of the Ti XXI $K\alpha$ line. Left and right scales on the ordinate in (b) give the center position of the Ti XXI $K\alpha$ line in channel numbers and the wavelength shift and toroidal plasma rotation velocity, respectively, relative to the center position of the Ti XXI $K\alpha$ line in the Ohmic heating phase. The wavelength shift, which is observed at the beginning of the discharge from 0.0 to 0.5 sec while the electron temperature is rising, corresponds to the expected dielectronic wavelength shift.

from the neutral beams. The decay after beams are turned off at 2.8 sec can be well represented by an exponential function which gives a characteristic momentum confinement time of 0.3 sec. The rotation velocity varies with beam power, electron density, and minor plasma radius. A study of these dependencies is important for tokamak experiments. The maximum rotation velocity observed to date is 6×10^7 cm/s for 5-MW deuterium beam injection into hydrogen plasmas. The small wavelength shift observed at the beginning of the discharge while the electron temperature is still rising to the saturation value is of the order of the dielectronic red shift shown in Fig. 6. It corresponds to the change of the line center position which one would expect from unresolved dielectronic satellites for an increase of the electron temperature from 1 to 2 keV. Corrections for this effect to the Doppler-shift measurements can be determined from calculations such as those in Fig. 6, using the measured electron temperature. The corrections are especially im-

portant if the rotation velocities are of the order of 1×10^6 cm/s.

The Doppler measurements which have been described so far do not depend on special properties of the Ti XXI spectrum. In the following we discuss diagnostic applications of the Ti XXI satellite spectrum. These spectral features are determined by the processes of dielectronic recombination and collisional inner-shell excitation, which are of fundamental importance for the spectra of multiply charged high-Z ions. In Sec. III we presented a detailed comparison between experimental observations and theoretical predictions and obtained excellent agreement for the entire satellite spectrum. In particular, we derived values for the electron temperature T_e and the ratio $N_{\text{Ti XX}}/N_{\text{Ti XXI}}$ of the abundances of lithiumlike and heliumlike titanium from a least-squares fit of a theoretical spectrum to the experimental data. Here we discuss these results.

The observed intensities represent line integrals of emissivity profiles along a central radial chord through the TFTR plasma. The emissivity profiles are determined by the radial distribution of the titanium charge states and by the radial electron density and electron temperature profiles. The charge-state distribution is described only approximately by the coronal equilibrium distribution. Deviations occur as a result of radial ion transport and charge-exchange recombination. These effects are not included in the coronal equilibrium curve of Fig. 10. In order to interpret the data in Fig. 10, we have modeled the plasma using the Multiple Impurity Species Transport (MIST) code.[52] The code takes into account diffusive and convective transport and calculates the ion charge-state distribution from theoretically predicted rate coefficients for the ionization and recombination processes. Radial emissivity profiles are then calculated from the resulting radial distribution of the titanium charge states.

Figure 14(a) shows computed radial density profiles of lithiumlike, heliumlike, and hydrogenlike titanium for (1) coronal equilibrium conditions (dashed curves) and for (2) a plasma with radial ion transport (solid curves). The radial particle transport flux, $\Gamma_q = -D\partial n_q/\partial r + v(r)n_q$, for each charge-state density n_q has been characterized by a diffusion coefficient of $D = 2\times10^4$ cm²/s and a convective transport parameter $c_v = 1$, where $v(r) = c_v D \partial(\ln n_e)/\partial r$.[53] Radial profiles of the form $n_e = n_e(0)[1-(r/a)^2]$ and $T_e = T_e(0)[1-(r/a)^2]^2$, with $n_e(0) = 3\times10^{19}$ m^{-3}, $T_e(0) = 1.8$ keV, and $a = 42$ cm, were assumed for the electron density and electron temperature, respectively. The value of $c_v = 1$ forces the total titanium density N_{Ti} to be proportional to the electron density in the central plasma region in steady state. Modifications due to charge-exchange recombination,[54] which depend on the poorly known neutral hydrogen density profile, are not included for the present illustrative case.

Figure 14(b) shows normalized emissivity profiles for the resonance line w, and for the satellites q and j. The emissivities for w and q were calculated from the expressions $\epsilon_w = \langle\sigma v\rangle_w n_e N_{\text{Ti XXI}}$ and $\epsilon_q = \langle\sigma v\rangle_q n_e N_{\text{Ti XX}}$, where $\langle\sigma v\rangle_w$ and $\langle\sigma v\rangle_q$ are the rate coefficients for direct electron impact excitation of Ti XXI and collisional inner-shell

excitation of Ti XX, respectively, as given in Table III of Ref. 1. Since these rate coefficients are very similar, the different widths of the emissivity profiles for lines w and q can be ascribed directly to the differences in the radial density distributions of the Ti XXI and Ti XX ions shown in Fig. 14(a). The emissivity of the line j, which is produced by dielectronic recombination of Ti XXI, is obtained from expression (7.1):
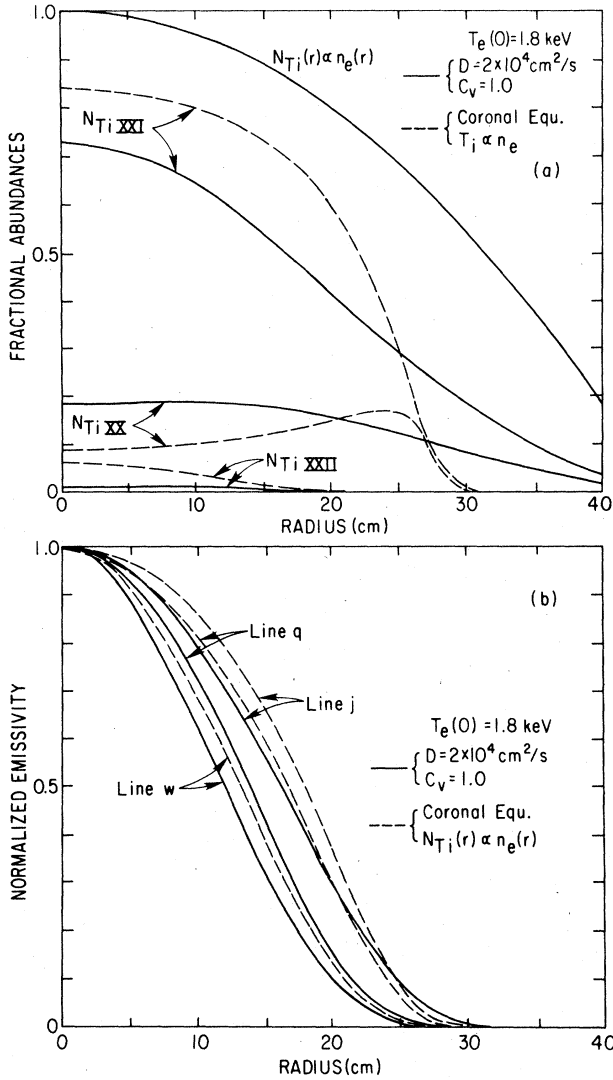

FIG. 14. (a) Radial density profiles of Ti XX, Ti XXI, and Ti XXII for (1) coronal equilibrium (dashed curves) and (2) a plasma with radial ion transport (solid curves). Profiles have been computed with use of the Multiple Ion Species Transport (MIST) code assuming electron density and temperature profiles of the form $n_e = n_e(0)[1 - (r/a)^2]$ and $T_e = T_e(0)[1 - (r/a)^2]^2$ with $n_e(0) = 3 \times 10^{19}$ m^{-3}, $T_e(0) = 1.8$ keV, and $a = 42$ cm. Transport is characterized by a diffusion coefficient $D = 2 \times 10^4$ cm^2/s and $c_v = 1$. (b) Emissivity profiles for the lines w, q, and j as calculated from the density and temperature profiles shown in (a).
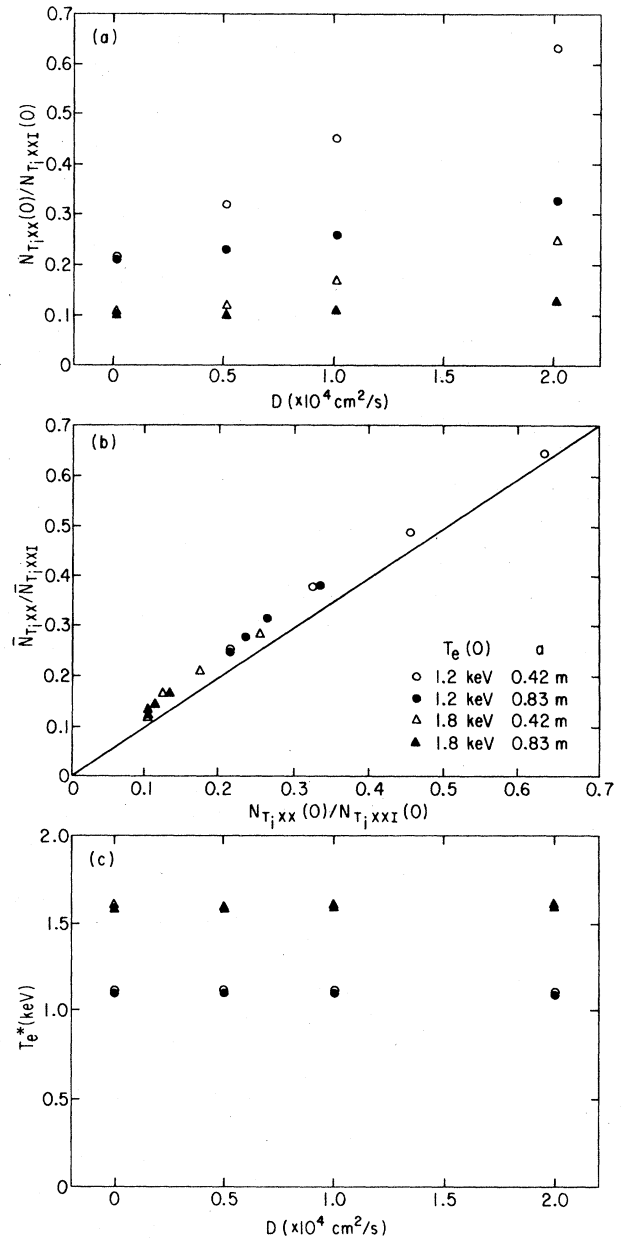

FIG. 15. (a) Central density ratios $N_{\text{Ti XX}}(0)/N_{\text{Ti XXI}}(0)$ as a function of the transport parameter D. Ratios have been computed with use of the MIST code for two values of central electron temperatures, $T_e(0) = 1.2$ and 1.8 keV, and plasma radii, $a = 42$ and 83 cm. Electron density and temperature profiles were of the form described in Fig. 14. $D = 0$ corresponds to coronal equilibrium. (b) Ratios of line-averaged charge-state densities vs the ratios of the central densities shown in (a). Line-averaged densities have been computed from line integrals of emissivity profiles. Solid line represents the case $\bar{N}_{\text{Ti XX}}(0)/\bar{N}_{\text{Ti XXI}}(0) = N_{\text{Ti XX}}(0)/N_{\text{Ti XXI}}(0)$. (c) Electron temperature values T_e^* as calculated from the ratio of line-integrated emissivities of j and w vs transport parameter D for the profiles discussed in (a). T_e^* values are nearly independent of D and close to 1.1 and 1.6 keV for two central electron temperatures of $T_e(0) = 1.2$ and 1.8 keV, respectively.

$$\epsilon_j = 3.3 \times 10^{-24} n_e N_{\mathrm{Ti\,XXI}} \left[\frac{E_{\mathrm{H}}}{T_e} \right]^{3/2}$$

$$\times \frac{g_j}{g_1} \frac{A_a A_r}{\sum A_r + A_a} \exp(-E_j/kT_e) , \qquad (8.1)$$

where $E_{\mathrm{H}} = 0.0136$ keV. Since the lines j and w both originate from heliumlike titanium, the differences in the emissivity profiles of j and w result from the different dependence of the rate coefficients on electron temperature. The emissivity profiles of lines w, q, and j are peaked at the center $(r=0)$ even for the case of coronal equilibrium where the density $N_{\mathrm{Ti\,XX}}$ of lithiumlike titanium is peaked off axis. This indicates that the lines are emitted mainly from the hot core of the plasma, with the emissivity profiles of w, q, and j less affected by radial transport than the ion density profiles shown in Fig. 14(a). Therefore, the observed intensities, which represent line integrals of the emissivity profiles, are essentially determined by the central plasma parameters. Transport, and other effects, may affect the detailed interpretation of the observed ratios, as discussed below.

Figure 15(a) shows the central density ratios $N_{\mathrm{Ti\,XX}}(0)/N_{\mathrm{Ti\,XXI}}(0)$ from calculated radial profiles of lithiumlike and heliumlike titanium as a function of the diffusion coefficient for $0 < D < 2 \times 10^4$ cm^2/s for two central electron temperatures, $T_e(0) = 1.2$ and 1.8 keV, and two plasma radii, $a = 42$ and 83 cm. $D = 0$ corresponds to coronal equilibrium. The dependence of $N_{\mathrm{Ti\,XX}}(0)/N_{\mathrm{Ti\,XXI}}(0)$ on the transport parameter D is stronger for plasmas with $a = 42$ cm than for plasmas with $a = 83$ cm due to the scaling of the gradients with minor plasma radius. The values of $N_{\mathrm{Ti\,XX}}(0)/N_{\mathrm{Ti\,XXI}}(0)$ are 2 or 3 times larger than the coronal equilibrium values for plasmas with $a = 42$ cm (and $D = 2 \times 10^4$ cm^2/s), whereas the deviations of $N_{\mathrm{Ti\,XX}}(0)/N_{\mathrm{Ti\,XXI}}(0)$ from coronal equilibrium are only 30% for plasmas with $a = 83$ cm.

Figure 15(b) shows density ratios $\overline{N}_{\mathrm{Ti\,XX}}/\overline{N}_{\mathrm{Ti\,XXI}}$ derived from the ratio of line integrals of the emissivity profiles of q and w, as a function of the central density ratios $N_{\mathrm{Ti\,XX}}(0)/N_{\mathrm{Ti\,XXI}}(0)$ shown in Fig. 15(a). The solid line represents the case $\overline{N}_{\mathrm{Ti\,XX}}/\overline{N}_{\mathrm{Ti\,XXI}} = N_{\mathrm{Ti\,XX}}(0)/N_{\mathrm{Ti\,XXI}}(0)$. The ratios $\overline{N}_{\mathrm{Ti\,XX}}/\overline{N}_{\mathrm{Ti\,XXI}}$ are somewhat larger but close to the central $N_{\mathrm{Ti\,XX}}(0)/N_{\mathrm{Ti\,XXI}}(0)$ values for the whole range of D values. We may conclude, therefore, that interpretation of the observed intensity ratio of the lines q and w is not very sensitive to changes of the radial profiles by transport and yields the central density ratio $N_{\mathrm{Ti\,XX}}(0)/N_{\mathrm{Ti\,XXI}}(0)$ to a good approximation.

Figure 15(c) presents values of the electron temperature, $\overline{T}_e$, derived from the ratio of the line-integrated emissivities of j and w as a function of D. The $\overline{T}_e$ values are nearly independent of D and close to 1.1 and 1.6 keV, for the corresponding central electron temperature values of 1.2 and 1.8 keV. We see that the electron temperature values, $\overline{T}_e$, which are derived from the observed intensity ratio of j and w, are insensitive to transport effects except for underestimating the central electron temperature $T_e(0)$ by $\sim 10\%$ in this range of $T_e(0)$ values.

With the appropriate corrections, such as those described in Figs. 15(b) and 15(c), we can interpret the experimental results shown in Fig. 10 as central values of $N_{\mathrm{Ti\,XX}}/N_{\mathrm{Ti\,XXI}}$ and T_e. In general, for reliable results, modeling of the impurity behavior and x-ray emission must be carried out for each plasma condition under study. The behavior shown in Fig. 15 should be representative of the required corrections except for plasmas with particularly strong or weak temperature gradients. The experimental values of $N_{\mathrm{Ti\,XX}}/N_{\mathrm{Ti\,XXI}}$ are significantly larger than the values expected for coronal equilibrium, in qualitative agreement with the effects of particle transport[52,53] and charge-exchange recombination with neutral hydrogen[54] on impurity ionization balances in tokamak plasmas. However, we also note that the details of any ionization balance depend sensitively on the total ionization and recombination rates for each ion, and remaining uncertainties in our quantitative knowledge of these processes must also be considered. For example, the ionization rates available from Younger[55] for certain neighboring elements are somewhat smaller than corresponding rates due to Lotz[50] or those from the atomic data calculations used here.[52] In this regard, it is interesting to note that deviations from coronal equilibrium similar to those shown in Fig. 10 were also observed in solar flares.[10] Here, transport and charge-exchange effects are presumably absent, and hence deviations from coronal equilibrium may more directly be ascribed to uncertainties in these atomic rates. For the present tokamak data, the presence of transport and charge-exchange processes allows us only to demonstrate that general agreement between the experimental data and the modeling calculations can be obtained within a range of plausible assumptions. More detailed analysis would have required plasma data beyond that available for these discharges. As an example, Fig. 10 includes model-derived data points in the range $0.8 < T_e(0) < 2.2$ keV, with $n_e(0) = 1 \times 10^{19}$ m^{-3}, $D = 1 \times 10^4$ cm^2/s, $c_v = 1$, and a central ratio of $n_{\mathrm{H^0}}/n_e = 10^{-6}$ for the neutral hydrogen and electron densities. Similar results can be obtained for other combinations of charge-exchange recombination, transport, and choice of theoretical ionization rates. The lack of a strong dependence on plasma minor radius in the data points of Fig. 10, however, indicates that transport alone probably is not responsible for the entire discrepancy between the data and the coronal equilibrium curve shown. The bracketed range of the model-derived points corresponds to choosing $42 < a < 83$ cm. Thus, the data can be accommodated with a theoretical model of the impurity transport and other processes to within the current understanding. Indeed, it appears that the experimental uncertainties in the determination of $T_e(0)$ and $N_{\mathrm{Ti\,XX}}(0)/N_{\mathrm{Ti\,XXI}}(0)$ are less of a problem than uncertainties in the impurity transport and other physics needed for the model.

A further application is the measurement of the dielectronic recombination rate coefficient of Ti XXI from the intensity of all of the dielectronic satellites relative to the intensity of the resonance line. This has been discussed previously for Fe XXV (Ref. 56). It is evident from Sec. III that these measurements confirm the current theoretical predictions for the dielectronic recombination rate coefficient.

IX. CONCLUSION

Satellite spectra of heliumlike titanium, Ti XXI, have been observed from TFTR tokamak plasmas with high spectral resolution ($\lambda/\Delta\lambda = 25\,000$ at $\lambda = 2.61$ Å). The spectra have been used for a detailed comparison with theoretical predictions and for diagnosis of central plasma parameters. In detail, we obtained the following results.

(1) The theoretical predictions for the spectrum of the Ti XXI resonance line and the associated lithiumlike and berylliumlike satellites in the wavelength range from 2.6000 to 2.6400 Å are in excellent agreement with the experimental observations. This indicates that the satellite features are satisfactorily described by the two theoretically considered processes of dielectronic recombination and collisional inner-shell excitation.

(2) The observed intensity ratios, I_x/I_w, I_y/I_w, and I_z/I_w, of the intercombination and forbidden lines and the resonance line are not in full agreement with the current theory. Partial agreement between the theoretical predictions and the observations is obtained for central electron temperatures in the range from 1.2 to 2 keV, where heliumlike titanium is the dominant state of ionization. In this range of electron temperatures, the sum of the observed intensity ratios, $G = (I_x + I_y + I_z)/I_w$, is well described by the value predicted for electron impact excitation (which includes contributions from direct excitation, radiative cascades, and collisional resonances) of Ti XXI. Discrepancies between theory and experiment by as much as an order of magnitude are observed, however, for $T_e(0) < 1.2$ keV. These discrepancies cannot be explained by the theoretically predicted contributions from inner-shell ionization of Ti XX and recombination of Ti XXII or an enhancement of the observed line intensities of x, y, and z due to the presence of unresolved lithiumlike and berylliumlike satellites. The data show a strong correlation between I_x/I_w, I_y/I_w, and I_z/I_w, and the ratio $N_{\mathrm{Ti\,xx}}/N_{\mathrm{Ti\,xxi}}$ of the abundances of lithiumlike and heliumlike titanium.

(3) The experimental and theoretical wavelengths agree to within the uncertainty of 0.5 mÅ of the calculations which include relativistic and radiative corrections up to third order in α. Wavelength shifts of the apparent resonance line profile due to contributions from unresolved dielectronic satellites have been determined as a function of the electron and ion temperature, and the fitting limits. These dielectronic wavelength shifts are important corrections to Doppler-shift measurements if the measured plasma velocities are of the order of 1×10^6 cm/s.

(4) Values of T_e and $N_{\mathrm{Ti\,xx}}/N_{\mathrm{Ti\,xxi}}$, the electron temperature and the ratio of the lithiumlike and heliumlike charge-state densities, were derived from a least-squares fit of a theoretical spectrum to the experimental data. Plasma modeling calculations show that these values represent the central parameters $T_e(0)$ and $N_{\mathrm{Ti\,xx}}(0)/N_{\mathrm{Ti\,xxi}}(0)$ to a good approximation even if the charge-state distribution deviates significantly from coronal equilibrium as a result of radial ion transport. The spectra can thus be used as a diagnostic of these central parameters.

(5) The observed ratios $N_{\mathrm{Ti\,xx}}/N_{\mathrm{Ti\,xxi}}$ are larger by factors of 2–3 than the central values $N_{\mathrm{Ti\,xx}}(0)/N_{\mathrm{Ti\,xxi}}(0)$ expected for coronal equilibrium. Agreement between the experimental data and the plasma modeling can be obtained by including particle transport and an estimated contribution from charge-exchange recombination. In principle, the spectra could be used as a diagnostic of the central neutral hydrogen density or impurity transport coefficients. Determination of these quantities is difficult, however, given the complex interaction of the various processes. Uncertainties in the assumed ionization rates and recombination rates should also be considered in the analysis.

(6) The central ion temperature and the central plasma rotation velocity of TFTR plasmas with auxiliary neutral beam heating have been determined from measurements of the Doppler broadening and Doppler shift of the Ti XXI resonance line. The observed rotation velocities are in reasonable agreement with values expected from the input torque to the plasma from the neutral beams. A momentum confinement time of 0.3 sec is deduced from the observed exponential decay of the rotation velocity after neutral beam injection.

(7) Rate coefficients for the dielectronic recombination of Ti XXI can be obtained from measurement of the total intensity of the dielectronic satellites relative to the intensity of the resonance line. It is evident from the discussion in Sec. III that the experimental data confirm the current theoretical predictions for the dielectronic recombination rate coefficient of Ti XXI.

The experimental results have been carefully documented to stimulate further theoretical analyses of the still existing discrepancies between the predicted and observed intensities of the intercombination and forbidden lines of Ti XXI.

Note added in proof. During the preparation of this article we learned that spectra of Ti XXI were also observed by Lee *et al.* from plasmas of the Doublet III tokamak.[57-59] The spectra of Lee *et al.* are in good agreement with our experimental results in those cases where the plasma parameters are comparable. The interpretation of some of their data, e.g., the use of the lines x, y, z, and w for diagnosis of the electron energy distribution, however, may have to be reconsidered in view of the still existing uncertainties about the excitation mechanisms for these lines in tokamak plasmas. Also, their measurements of toroidal plasma rotation velocities from the *apparent* resonance line w may be subject to corrections, since the observed wavelength shifts are comparable with the dielectronic red shifts due to unresolved satellites. These wavelength shifts have been quantiatively determined in Sec. IV of this paper. The present paper also includes new results on the contributions from berylliumlike satellites.

[1] F. Bely-Dubau, P. Faucher, L. Steenman-Clark, M. Bitter, S. von Goeler, K. W. Hill, C. Camhy-Val, and J. Dubau, Phys. Rev. A **26**, 3459 (1982).

[2] M. Bitter, S. von Goeler, S. Cohen, K. W. Hill, S. Sesnic, F. Tenney, J. Timberlake, U. I. Safronova, L. A. Vainshtein, J. Dubau, M. Loulergue, F. Bely-Dubau, and L. Steenman-Clark, Phys. Rev. A **29**, 661 (1984).

[3] F. Bely-Dubau, J. Dubau, P. Faucher, A. H. Gabriel, M. Loulergue, L. Steenman-Clark, S. Volonté, E. Antonucci, and C. G. Rapley, Mon. Not. R. Astron. Soc. **201**, 1155 (1982).

[4] P. Faucher, M. Loulergue, L. Steenman-Clark, and S. Volonté, Astron. Astrophys. **118**, 147 (1983).

[5] E. Källne, J. Källne, and A. K. Pradhan, Phys. Rev. A **28**, 467 (1983).

[6] E. Källne, J. Källne, and A. Dalgarno, E. S. Marmar, J. E. Rice, and A. K. Pradhan, Phys. Rev. Lett. **52**, 2245 (1984).

[7] U. I. Safronova, A. M. Urnov, and L. A. Vainshtein, Proc. P. N. Lebedev Phys. Inst. [Acad. Sci. USSR **119**, 13 (1980)].

[8] Y. I. Grineva, V. I. Karov, V. V. Korneev, V. V. Krutov, S. L. Mandelstam, L. A. Vainshtein, B. N. Vasilysev, and J. A. Zhitnik, Sol. Phys. **29**, 441 (1973).

[9] A. H. Gabriel, J. L. Culhane, L. W. Acton, E. Antonucci, R. D. Bentley, C. Jordan, L. W. Leibacher, A. N. Parmar, K. J. H. Phillips, C. G. Rapley, C. J. Wolfson, and K. T. Strong, Adv. Space Res. **1**, 267 (1981).

[10] E. Antonucci, A. H. Gabriel, J. G. Doyle, J. Dubau, P. Faucher, C. Jordan, and N. Veck, Astron. Astrophys. **133**, 239 (1984).

[11] E. Antonucci, A. H. Gabriel, L. W. Acton, J. L. Culhane, J. G. Doyle, J. W. Leibacher, M. E. Machado, L. E. Orwig, and G. Rapley, Sol. Phys. **78**, 107 (1982).

[12] A. N. Parmar, J. L. Culhane, C. G. Rapley, E. Antonucci, A. H. Gabriel, and M. Loulergue, Mon. Not. R. Astron. Soc. **197**, 29P (1981).

[13] N. J. Peacock, H. P. Summers, J. Phys. B **11**, 3757 (1978).

[14] K. W. Hill, S. von Goeler, M. Bitter, L. Campbell, R. D. Cowan, B. Fraenkel, A. Greenberger, R. Horton, J. Hovey, W. Roney, N. R. Sauthoff, and W. Stodiek, Phys. Rev. A **19**, 1770 (1979).

[15] M. Bitter, S. von Goeler, R. Horton, M. Goldman, K. W. Hill, N. R. Sauthoff, and W. Stodiek, Phys. Rev. Lett. **42**, 304 (1979).

[16] TFR Group, J. Dubau, and M. Loulergue, J. Phys. B **15**, 1007 (1981).

[17] M. Bitter, K. W. Hill, N. R. Sauthoff, P. C. Efthimion, E. Meservey, W. Roney, S. von Goeler, R. Horton, and W. Stodiek, Phys. Rev. Lett. **43**, 129 (1979).

[18] M. Bitter, S. von Goeler, K. W. Hill, R. Horton, D. W. Johnson, W. Roney, N. R. Sauthoff, E. H. Silver, and W. Stodiek, Phys. Rev. Lett. **47**, 921 (1981).

[19] M. Bitter, S. von Goeler, M. Goldman, K. W. Hill, R. Horton, W. Roney, N. Sauthoff, and W. Stodiek, in *Temperature, Its Measurement and Control in Science and Industry,* edited by J. F. Schooley (AIP, New York, 1982), Vol. 5, p. 693.

[20] M. Bitter, S. von Goeler, K. Hill, K. Brau, D. Eames, M. Goldman, E. Silver, and W. Stodiek, in *Inner-Shell and X-Ray Physics of Atoms and Solids,* edited by D. J. Fabian, H. Kleinpoppen, and L. M. Watson (Plenum, New York, 1981), p. 861.

[21] A. H. Gabriel and C. Jordan, in *Case Studies in Atomic Collision Physics,* edited by E. W. McDaniel and M. R. C. McDowell (North-Holland, Amsterdam, 1972), Vol. 2, p. 211.

[22] L. W. Acton and W. A. Brown, Astrophys. J. **225**, 1065 (1978).

[23] K. W. Hill *et al.*, Rev. Sci. Instrum. **56**, 840 (1985).

[24] K. W. Hill *et al.*, 6th Topical Meeting on the Technology of Fusion Energy, San Francisco, 1985 (unpublished).

[25] C. Breton, C. De Michelis, M. Finkenthal, and M. Mattioli, Fontenay-aux-Roses Laboratory Report No. EUR-CEA-FC-948, 1978 (unpublished).

[26] H. Johann, Z. Phys. **69**, 189 (1931).

[27] K. W. Hill, M. Bitter, M. Tavernier, M. Diesso, S. von Goeler, G. Johnson, L. C. Johnson, N. R. Sauthoff, N. Schechtman, S. Sesnic, F. Tenney, and K. M. Young, Rev. Sci. Instrum. **56**, 1165 (1985).

[28] A. H. Gabriel, Mon. Not. R. Astron. Soc. **160**, 99 (1972).

[29] U. I. Safronova, Phys. Scr. **23**, 241 (1981).

[30] P. J. Mohr, Ann. Phys. (N.Y.) **88**, 26 (1974).

[31] P. J. Mohr, Phys. Rev. A **26**, 2238 (1982).

[32] R. K. Janev, L. P. Presnyakov, and V. P. Shevelko, in *Physics of Highly Charged Ions,* Vol. 13 of *Springer Series in Electrophysics,* edited by G. Ecker (Springer, Berlin, 1985).

[33] J. P. Briand, M. Tavernier, R. Marrus, H. Gould, and J. P. Desclaux, Phys. Rev. A **28**, 1413 (1983).

[34] G. R. Blumenthal, G. W. F. Drake, and W. H. Tucker, Astrophys. J. **172**, 205 (1972).

[35] R. Mewe and J. Schrijver, Astron. Astrophys. **65**, 99 (1978).

[36] R. Mewe and J. Schrijver, Astron. Astrophys. **65**, 115 (1978).

[37] R. Mewe and J. Schrijver, Astron. Astrophys. Suppl. **33**, 311 (1978).

[38] F. Bely-Dubau, J. Dubau, P. Faucher, and A. H. Gabriel, Mon. Not. R. Astron. Soc. **198**, 239 (1982).

[39] D. L. Kenzie and P. B. Landecker, Astrophys. J. **259**, 372 (1982).

[40] TFR Group, F. G. Doyle, and J. L. Schwob, J. Phys. B **15**, 813 (1982).

[41] A. K. Pradhan and J. M. Shull, Astrophys. J. **249**, 821 (1981).

[42] A. K. Pradhan, Astrophys. J. **288**, 824 (1985).

[43] R. W. P. McWhirter, in *Proceedings of the Course on Plasma Diagnostics and Data Acquisition Systems, Varenna, Italy, 1975,* edited by H. Eubank and E. Sindoni (Editrice Compositori, Bologna, 1975), pp. 178–243.

[44] Yong-Ki Kim (private communication).

[45] M. H. Chen, B. Crasemann, and H. Mark, Phys. Rev. A **24**, 1852 (1981).

[46] P. Faucher and J. Dubau, Phys. Rev. A **31**, 3672 (1985).

[47] D. M. Sampson, A. D. Park, and R. E. H. Clark, Phys. Rev. A **17**, 1619 (1978).

[48]TFR Group, F. Bombarda, F. Bely-Dubau, P. Faucher, M. Cornille, J. Dubau, and M. Loulergue, Phys. Rev. A 32, 2374 (1985).

[49]L. Steenman-Clark and P. Faucher, J. Phys. B 17, 73 (1984).

[50]W. Lotz, Astrophys. J. 14, 207 (1967).

[51]W. Eissner, M. Jones, and H. Nussbaumer, Comput. Phys. Commun. 8, 270 (1974).

[52]R. A. Hulse, Nuclear Technology/Fusion 3, 259 (1983).

[53]R. J. Fonck and R. A. Hulse, Phys. Rev. Lett. 52, 530 (1984).

[54]R. A. Hulse, D. E. Post, and D. R. Mikkelsen, J. Phys. B 13, 3895 (1980).

[55]S. M. Younger, J. Quant. Spectrosc. Radiat. Transfer 29, 61 (1983).

[56]F. Bely-Dubau, M. Bitter, J. Dubau, P. Faucher, A. H. Gabriel, K. W. Hill, S. von Goeler, N. Sauthoff, and S. Volonte, Phys. Lett. 93A, 189 (1983).

[57]P. Lee, A. J. Lieber, and S. S. Wojtowicz, Phys. Rev. A 31, 3996 (1985).

[58]P. Lee, A. J. Lieber, R. P. Chase, and A. K. Pradhan, Phys. Rev. Lett. 55, 386 (1985).

[59]A. J. Lieber, P. Lee, R. T. Snider, and S. S. Wojtowicz, G. A. Technologies, Inc. (San Diego) Report No. GA-A17880, 1985 (unpublished).